2013-06

Small flux buoy for characterizing marine surface layers

Zúñiga, Carlos A.

Monterey, California: Naval Postgraduate School

NAVAL POSTGRADUATE SCHOOL

MONTEREY, CALIFORNIA

THESIS

SMALL FLUX BUOY FOR CHARACTERIZING MARINE SURFACE LAYERS

by

Carlos A. Zúñiga

June 2013

Thesis Advisor: Qing Wang
Co-Advisor: Thomas Herbers

Approved for public release; distribution is unlimited

THIS PAGE INTENTIONALLY LEFT BLANK

REPORT DOCUMENTATION PAGE

Form Approved OMB No. 0704–0188

1. AGENCY USE ONLY *(Leave blank)*	**2. REPORT DATE** June 2013	**3. REPORT TYPE AND DATES COVERED** Master's Thesis

4. TITLE AND SUBTITLE
SMALL FLUX BUOY FOR CHARACTERIZING MARINE SURFACE LAYERS

5. FUNDING NUMBERS

6. AUTHOR(S) Carlos A. Zúñiga

7. PERFORMING ORGANIZATION NAME(S) AND ADDRESS(ES)
Naval Postgraduate School
Monterey, CA 93943–5000

8. PERFORMING ORGANIZATION REPORT NUMBER

9. SPONSORING /MONITORING AGENCY NAME(S) AND ADDRESS(ES)
N/A

10. SPONSORING/MONITORING AGENCY REPORT NUMBER

11. SUPPLEMENTARY NOTES The views expressed in this thesis are those of the author and do not reflect the official policy or position of the Department of Defense or the U.S. Government. IRB Protocol number ____N/A____.

12a. DISTRIBUTION / AVAILABILITY STATEMENT
Approved for public release; distribution is unlimited

12b. DISTRIBUTION CODE

13. ABSTRACT (maximum 200 words)

A small easily deployable buoy, Marine-Air-Sea-Flux System (MASFlux), has been developed by the Meteorology Department of the Naval Postgraduate School. This system measures turbulence perturbations, mean wind and thermodynamic profiles, surface wave, and upper ocean temperature simultaneously. This research focuses on testing, documenting, and evaluating the MASFlux performance. The buoy system was tested in the Monterey Bay since August 2012 using small vessels, with the first three deployments focusing on sensor and buoy performance improvements. Concurrent measurements of wave and turbulence fluxes in the lower part of the atmospheric boundary layer during the last three deployments were not subject to apparent sensor errors or excessive mast rotations. Data from these deployments are analyzed here. The two-dimensional wave measurements were compared with those from the Datawell DWR-G4 wave buoys and showed consistent results in all deployments. Turbulent spectra analyses for data before and after buoy motion correction demonstrate the effectiveness in motion correction for the MASFlux. The spectra revealed a significant amount of energy in the atmospheric turbulence at frequencies of the dominant swell. The mean vertical wind profiles also indicated the effects of swell. These initial measurements and results point to great potential for the MASFlux for future air-sea-wave study.

14. SUBJECT TERMS Air-sea interaction, wave and fluxes concurrent measurements, small buoy	**15. NUMBER OF PAGES** 85
	16. PRICE CODE

17. SECURITY CLASSIFICATION OF REPORT	**18. SECURITY CLASSIFICATION OF THIS PAGE**	**19. SECURITY CLASSIFICATION OF ABSTRACT**	**20. LIMITATION OF ABSTRACT**
Unclassified	Unclassified	Unclassified	UU

NSN 7540–01–280–5500

Standard Form 298 (Rev. 2–89)
Prescribed by ANSI Std. 239–18

THIS PAGE INTENTIONALLY LEFT BLANK

Approved for public release; distribution is unlimited

SMALL FLUX BUOY FOR CHARACTERIZING MARINE SURFACE LAYERS

Carlos A. Zúñiga
Lieutenant, Chilean Navy
B.S., Academia Politecnica Naval, 2006

Submitted in partial fulfillment of the
requirements for the degree of

MASTER OF SCIENCE IN PHYSICAL OCEANOGRAPHY

from the

NAVAL POSTGRADUATE SCHOOL
June 2013

Author: Carlos A. Zúñiga

Approved by: Qing Wang
Thesis Advisor

Thomas Herbers
Thesis Co-Advisor

Peter Chu
Chair, Department of Oceanography

THIS PAGE INTENTIONALLY LEFT BLANK

ABSTRACT

A small easily deployable buoy, Marine-Air-Sea-Flux System (MASFlux), has been developed by the Meteorology Department of the Naval Postgraduate School. This system measures turbulence perturbations, mean wind and thermodynamic profiles, surface wave, and upper ocean temperature simultaneously. This research focuses on testing, documenting, and evaluating the MASFlux performance. The buoy system was tested in the Monterey Bay since August 2012 using small vessels, with the first three deployments focusing on sensor and buoy performance improvements. Concurrent measurements of wave and turbulence fluxes in the lower part of the atmospheric boundary layer during the last three deployments were not subject to apparent sensor errors or excessive mast rotations. Data from these deployments are analyzed here. The two-dimensional wave measurements were compared with those from the Datawell DWR-G4 wave buoys and showed consistent results in all deployments. Turbulent spectra analyses for data before and after buoy motion correction demonstrate the effectiveness in motion correction for the MASFlux. The spectra revealed a significant amount of energy in the atmospheric turbulence at frequencies of the dominant swell. The mean vertical wind profiles also indicated the effects of swell. These initial measurements and results point to great potential for the MASFlux for future air-sea-wave study.

THIS PAGE INTENTIONALLY LEFT BLANK

TABLE OF CONTENTS

LIST OF FIGURES

LIST OF TABLES

THIS PAGE INTENTIONALLY LEFT BLANK

LIST OF ACRONYMS AND ABBREVIATIONS

ABL	Atmospheric Boundary Layer
AREPS	Fleet the Advanced Refractive Effects Prediction System
ASIS	Air-Sea Interaction Spar
ECM	Eddy Correlation Method
FB	Naval Postgraduate School Flux Buoy
FLIP	Floating Instrument Platform
FS	Full Scale
GPS	Global Positioning System
MABL	Marine Atmospheric Boundary Layer
MOAS	Met-On-A-Stick
MOST	Monin-Obukhov Similarity Theory
NOAA	National Oceanic and Atmospheric Administration
NDBC	National Data Buoy Center
NPS	Naval Postgraduate School
U_{10}	Wind Measurement 10 m Above the Sea Level
OBL	Oceanic Boundary Layer
PPS	Pulse Per Second
P-M	Pierson and Maskowitz Spectrum
q	Water Vapor
RH	Relative Humidity
SWH	Significant Wave Height

THIS PAGE INTENTIONALLY LEFT BLANK

ACKNOWLEDGMENTS

Firstly I would like to express all my gratitude to my advisor, Dr. Qing Wang, for her priceless and selfless contribution and guidance throughout this thesis research. Her bright ideas and tremendous knowledge make the Naval Postgraduate School a more prestigious institution. Also my deep gratitude goes to Mr. Richard Lind, who made me part of this project since the very beginning–from the sketch of the buoy until the final prototype presented in this research.

I would like to recognize Dr. Thomas Herbers and Mr. Paul Jessen for all their help especially during the waves analysis results and also their coordination that made possible several test deployments in Monterey Bay.

An important part of this research was made thanks to Dr. John Kalogiros' advice, particularly during calibrations and test control of the collected data. His experience in turbulence and wave measurements was important in the final product analyzed.

To the National Oceanic and Atmospheric Administration (NOAA) and especially to the crew of the Monterey Bay National Marine Sanctuary ships, for their support and professionalism during all the time spent at the sea for testing deployments.

It is important to acknowledge the Chilean Navy and particularly the Hydrographic and Oceanographic Office Institution which trusted my capabilities and gave me the opportunity to improve my knowledge in the ocean sciences.

Finally, and most importantly, I would like to thank my wife, Michelle, my son, Martin, and daughter, Barbara, for being such great partners in this unforgettable journey. They recharged my batteries daily and encouraged me to be a better person, father, and student.

THIS PAGE INTENTIONALLY LEFT BLANK

I. INTRODUCTION

A. THE NEED FOR NEAR-SURFACE FLUX-WAVE MEASUREMENTS

The momentum, heat, water vapor, and gas exchange at the air-sea interface is one of the key components in climate and weather forecast models. Such an exchange is represented by the so-called surface flux parameterization, which was largely developed based on Monin-Obukhov similarity theory (MOST). The empirical relationship embedded in MOST were originally developed from results obtained during the famous Kansas experiment (Businger et al. 1971) where measurements were made over a flat, homogeneous, cut grass area. The state-of-the-art surface flux parameterization is the Coupled Ocean-Atmosphere Response Experiment (COARE) algorithm (Fairall et al. 1996, 2003), made further improvement based on a large number of data, particularly those from over the ocean. Such an algorithm has been implemented in many forecast models.

It has been recognized over recent years that coupled atmosphere, wave, and ocean models provide more realistic forecasts in some conditions, such as under strong gap wind in the Gulf of Tehuantepec (Hornick 2012) or in hurricane conditions. The availability of wave parameters from coupled models calls for surface flux parameterizations utilizing wave parameters, specifically the sea-state dependent surface flux parameterizations. The current MOST-based parameterizations, including the COARE algorithm, do not include wave effect explicitly; although the wind wave effect is represented through roughness length parameterizations.

Sea-state dependent surface flux parameterizations have been developed in the past by many previous studies. However, this subject requires more in-depth study to enhance our understanding of the physical processes occurring at the air-sea-wave interface and subsequently to improve flux parameterizations. This particular application requires concurrent and co-located measurements of

surface fluxes and waves. To examine the applicability of the empirical relationship in MOST, one also needs to obtain mean measurements from at least two levels in the surface layer. Ideally, this needs to be done close to the surface within the lowest few meters to ~100 m, depending on the depth of the boundary layer. Since ship masts at the bow are normally above 10 m and can be ~20–30 m above the water level for large vessels, ship-based measurements are limited for this application. Furthermore, the flow distortion introduced by the ship superstructure also makes such measurements unreliable. Buoy-based measurements are, therefore, preferred.

Different types of flux buoys currently exist. The Air-Sea Interaction Spar (ASIS) buoy (Drennan et al. 2003) is probably the most appropriate for flux and wave measurements due to its unique design as a spar buoy. Other flux buoys, such as the one at the Naval Postgraduate School (NPS), use disc buoys 2–3 m diameter as the platform to set up the instruments at multiple levels. Although proving effective, the size and weight of the flux buoys make it difficult and costly to deploy and recover these buoys unless a large vessel is involved.

Recent developments in Global Position System (GPS) technology and sensor miniaturization allow us to develop a much smaller buoy with similar capability. The NPS developed a small buoy system, Met-On-A-Stick (MOAS), in 2010, which was discussed and evaluated in Cheney (2011). This measurement system has been improved to include direct flux measurement capability with a sonic anemometer at the top of the mast and better sensors for mean measurements with better precision. The new buoy system measures all variables simultaneously to include ocean waves, turbulent perturbations $(w', u' \text{and } \theta')$, and mean $(\overline{W}, \overline{U} \text{ and } \overline{\theta})$ for in-depth analyses of the flux-profile relationship. These new additions to MOAS prompt a new name for the instrumented buoy: marine-air-sea flux system (MASFlux). The MASFlux system has a total length of ~ 6 m and weighs 40 kg. This new buoy system has at the top an ultrasonic anemometer for turbulent perturbations and two levels for mean wind, temperature, and relative humidity measurements. It can also measure sea

temperature at several levels within 1 m below the ocean surface. Several at-sea tests of the new buoy system have been made in 2012 and 2013. This thesis research will analyze measurements from the buoy testing to understand the performance of the new flux buoy and the air-sea interaction revealed from the test measurements.

B. OBJECTIVES OF THIS THESIS

A near-surface measurement system previously developed at NPS, the MOAS, was improved with flux sampling capabilities. The goal of this thesis is to improve the representation of momentum and heat exchange at the air-sea interface using measurements from the MasFLUX deployed in the vicinity of Monterey Bay. Multiple buoy deployments from a small ship have been made in different wind/wave conditions. The resulting datasets will be evaluated for both data quality control and for surface flux parameterization analyses giving important information to be used in forecast and electromagnetic propagation models.

This thesis focuses on the design and testing of the NPS MASFlux buoy for air-sea interaction study. The ultimate goal is to develop an easily deployable buoy system that is capable of concurrent flux, profile, and surface wave measurements for future air-sea interaction study and, in the future, for sampling environmental conditions for electromagnetic wave propagation.

C. MILITARY APPLICATIONS

Accurate characterization and forecast of the environmental conditions are vital to military operation overland and at sea. Accurate representation of the surface flux and the surface layer processes are keys to forecast success. Moreover, the near surface temperature and moisture profiles affect the propagation of radar signals and hence sensor and communication. The following sections give more details of the specific impact areas.

1. Near Surface Profiles

The near surface profiles of temperature and moisture often result in conditions where radar signal propagation is confined in the lowest meters or hundred meters of the atmosphere, often referred to as the ‘evaporation duct’ or surface-based duct. Currently in the U.S. Navy, forecast of the radar wave propagation relies on the accuracy of the low-level vertical profiles with no in situ observations. This adds the pressure of improved boundary layer forecast, which can benefit from better understanding of the surface layer/boundary layer processes and better parameterizations. In research mode, measurements from the MASFlux can be used directly as ground truth for model validation and/or, when combined with measurements from higher levels, as input to the radar propagation model. Radar and communications operations will benefit, and also meteorologists and oceanographers could have more accurate tools enabling them to offer better advice in the operations areas. In terms of the first mentioned, its propagation is strongly influenced and often dominated by evaporative ducting (Frederickson and Davidson 2003), making it important to obtain as much as possible humidity profiles in the near surface.

2. Flux Parameterization

An accurate flux parameterization is essential to models on all scales and resolutions (Webster and Lukas 1992). As the forecast models move towards coupled air-ocean-wave forecasts, large amounts of data and cases are needed to improve the current flux parameterization to include sea state in different wave regimes, which can be obtained by the MASFlux. With this data, models and parameterization algorithms can be developed, improved, tested, and improved again as a loop to obtain the most refined information possible. This information will be delivered to fleets as needed.

Currently the Fleet uses the Advanced Refractive Effects Prediction System (AREPS) to assess radar propagation conditions, which are extremely sensitive to the measured data input (Frederickson and Davidson 2003). So,

rather than feeding this and other similar models the MOST estimated profiles as is usually done, it would be convenient to feed these models the measured humidity and temperature profiles, thereby avoiding errors in evaporation duct features.

THIS PAGE INTENTIONALLY LEFT BLANK

II. AIR-SEA INTERACTION OVER WAVE SURFACES

Air-sea interaction at the air-sea interface involves the adjacent boundary layers of both media: the atmospheric boundary layer and the ocean mixed layer. The thermal structure through the two boundary layers is shown schematically in Figure 1 (from Lykossov 2001). The turbulence exchange process at the interface is strongly influenced by the state of the sea surface. They are also regulated by the wind in the atmosphere and thermodynamics of both layers. The atmospheric flows that generate the surface flux issue is not an isolated characteristic of the sea surface state, but rather an indicator of the coupled atmospheric and oceanic boundary layer dynamics. In fact, the physical coupling between the atmosphere and the ocean is accomplished by the surface fluxes of momentum, heat, and gas exchanges.

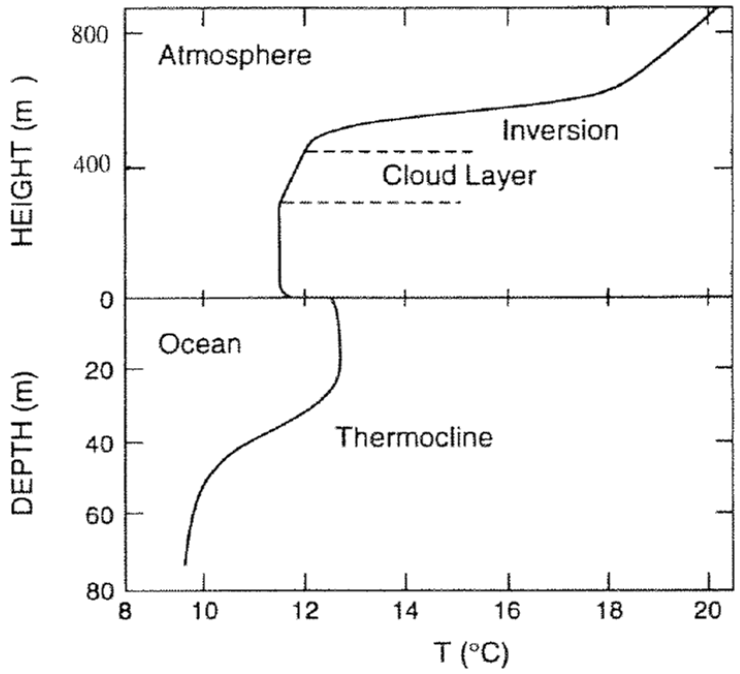

Figure 1. Typical thermal profile through the atmosphere and the upper ocean (from Lykossov 2001).

The presence of the boundary layer below the main inversion about 500 m is shown in Figure 1. The lowest 10% of the boundary layer is characterized by constant turbulence fluxes, where the vertical variation of fluxes is less than 10%. This thin layer, normally from meters to ~100 m in depth, is referred to as the surface layer. Surface flux parameterizations are mainly based on the physics of the surface layer to be discussed in Section A of this chapter. The oceanic boundary layer is the top layer above the thermocline. While the presence of a surface layer is rather obscure in the ocean, its contribution to the flux exchange is through surface waves to be discussed in Sections B and C of this chapter.

In this chapter, an overview is provided on the physics of flux exchanges at the air-sea interface over the wave field, from wind-generated waves, and from the effects of waves on surface fluxes (sections A, B, and C). The last section will provide an overview of existing flux/wave sampling systems similar to the one described in this thesis.

A. SURFACE FLUXES AND SURFACE FLUX PARAMETERIZATION

While air-sea interaction involves processes on a wide range of spatial and temporal scales, the transferring of momentum, heat, moisture, gas, and aerosols across the air-sea interface is governed by turbulent processes. Such turbulent transfer physically couples the atmosphere and the ocean. For models of any scale and complexity that intend to simulate the atmosphere-wave-ocean coupling processes, accurate parameterization of the interfacial turbulent fluxes using model-resolvable variables are necessary (e.g., Bao et al. 2000; Chen et al. 2010). The reliable estimates of the flux transfers are of primary importance for weather prediction and climate studies, for forecasting of waves and surges, and for many other meteorological and oceanographic applications. A brief review of our current understanding of the physics pertaining to turbulent transfer of momentum, sensible, and latent heat flux is given in this section.

The three fluxes of main concern for air-sea interaction subjects are momentum (or wind stress, τ), sensible heat (H_s), and latent heat (H_l) fluxes defined as:

$$\begin{aligned} \tau &= -\rho\overline{w'u'} = \rho u_*^2 \\ H_s &= \rho c_p \overline{w'\theta'} = -\rho c_p u_* \theta_* \\ H_l &= \rho L_v \overline{w'q'} = -\rho L_v u_* q_* \end{aligned} \tag{0.1}$$

where u', w', q', and θ' are turbulent perturbations of the stream-wise component horizontal wind, vertical velocity, specific humidity, and potential temperature, respectively. The bars denote Reynolds averages, c_p is the specific heat for dry air at constant pressure, ρ is density, and L_v is the latent heat of vaporization. The variables u_*, q_*, and θ_* are velocity, water vapor, and temperature scales that are defined based on the respective kinematic fluxes.

Based on Monin-Obukhov similarity theory (hereafter MOST, Monin and Obukhov 1954), non-dimensional gradient of wind, temperature, and humidity in the surface layer can be written as:

$$\begin{aligned} \frac{kz}{u_*}\frac{\partial u}{\partial z} &= \phi_m\left(z/L\right) \\ \frac{kz}{\theta_*}\frac{\partial \theta}{\partial z} &= \phi_h\left(z/L\right) \\ \frac{kz}{q_*}\frac{\partial q}{\partial z} &= \phi_q\left(z/L\right) \end{aligned} \tag{0.2}$$

where L is the Monin-Obukhov length defined as $L = \frac{u_*^3\theta}{kg\overline{w'\theta'}}$, ϕ_m, ϕ_h, and ϕ_q, are empirical non-dimensional gradients for the corresponding variables and are functions of z/L. The ϕ functions denote the effects of the thermal stability in the surface layer. In neutral thermal stability $\phi_m(0) = 1$ for momentum, yielding the famous log-wind profile. The most frequently used non-dimensional gradient functions are those derived from the Kansas experiment (Businger et al. 1971).

The bulk aerodynamic flux parameterization was derived based on the surface layer similarity theory given in Equation 2.2. We define a drag coefficient $C_D = \left(\frac{u_*}{\overline{u}}\right)^2$. In neutral conditions, the drag coefficient at 10 m height can be written as:

$$C_{DN} = \left(\frac{k}{\ln(10/z_0)}\right)^2 \tag{0.3}$$

where z_0 is the surface roughness defined as the height where mean wind becomes zero. Similarly, we can define the exchange coefficient $C_H = \frac{\theta_*}{\overline{\theta_{10}} - \overline{\theta_{z_0}}} C_D^{1/2}$, and $C_q = \frac{q_*}{\overline{q_{10}} - \overline{q_{z_0}}} C_D^{1/2}$ for sensible and latent heat, respectively; the surface fluxes, expressed in terms of drag and exchange coefficients are given by:

$$\begin{aligned} \overline{u'w'} &= -C_D \overline{U_{10}}^2 \\ \overline{w'\theta'} &= -C_H \overline{U_{10}}\left(\overline{\theta_{10}} - \overline{\theta_0}\right) \\ \overline{w'q'} &= -C_q \overline{U_{10}}\left(\overline{q_{10}} - \overline{q_0}\right) \end{aligned} \tag{0.4}$$

Equation 2.4 is the bulk aerodynamic parameterization that provides estimates of kinematic surface fluxes using the mean wind, temperature, and specific humidity at 10 m height and at the surface (z_0 level). The key parameters involved in the bulk flux parameterization are the drag and exchange coefficients and the surface roughness length; the latter uniquely determines the drag coefficient in neutral conditions (Equation 2.3). Thus, the objective of improving flux parameterization is to find an accurate representation of drag/exchange coefficients, or z_0.

B. WIND GENERATED WAVES, WAVE AGE, AND SWELL

Ocean waves play an important role in the interaction of the atmosphere and ocean. On the one hand, ocean waves receive energy and momentum from the atmosphere through wind input. Hence, to a large extent, the ocean waves

control the drag of the air flow over the ocean. On the other hand, the ocean waves transfer energy and momentum to the ocean through the process of white capping; thereby feeding the turbulent and large-scale motions of the ocean.

The wind waves on the ocean surface are complicated enough so that no single idealized model can describe their growth rate as seen from observations. The issue is further complicated by the fact that accurate measurements to support wave growth theory are difficult to obtain, making direct model evaluation nearly impossible, or at best incomplete. Jones and Toba (2001) give a comprehensive overview on many different aspects of the wind-wave interaction process. Central to the discussions is the growth of waves under wind forcing characterized by 'wave age' to express the relative speed of the wind and the characteristic wind wave. Early in the development of a wave field, the characteristic wind-wave is of short length and travels more slowly than the wind at some height above the surface. The phase speed of the most energetic wind waves is denoted as c_p, which is at the peak of the wave slope spectrum. The term 'wave age' is defined as the ratio $c_p / U_{10N} \cos\theta$ where $U_{10N} \cos\theta$ is the component of wind speed at a 10 m reference height traveling in the direction of the waves, and θ is the difference between wind and wave propagation direction. The wave age concept was introduced to represent the developing stage of the young wave. As wind waves continue to develop, the characteristic frequency decreases and the speed of propagation increases until it becomes equal to the wind. When wave age reaches unity, the fast traveling waves become 'mature' waves, meaning that the growth of the wave would be small once it matures. Developing waves (or young waves) are commonly observed with atmospheric flow with changing wind direction or speed. They are also frequently found in fetch-limited offshore coastal flow. Young developing waves are dominated by the growth of high-frequency capillary waves and small gravity waves that ride on the top of long gravity waves. Since they travel more slowly than the wind, young developing waves act like 'form-drags' and lead to high surface stress (Donelan 1982; Geernaert et al. 1986).

An alternative quantitative wave age definition is the ratio c_p/u_* where u_* is the frictional velocity of the atmospheric surface layer. This definition of wave age is preferred because the use of u_* avoids taking into account the influence of stratification on the velocity profile and the issue of the appropriate height at which to measure the wind speed. With this velocity scale, a mature wind-wave has an age of about 30. With some research, the inverse wave age is used as well. Irrespective of the specific definition, wave age is a general measure which expresses the state of wind-wave development and is used to indicate conditions with respect to energy input, dissipation, and non-linear transfer in the wave field (Jones and Toba 2001).

When wind-waves are in local equilibrium with the wind, it is in a situation where some measure of the wind velocity, say u_*, is all that is necessary to characterize the forcing of the wind-waves. This is not the case with rapidly changing wind stress or direction. The concept of wind-wave equilibrium recognizes that the water boundary layer below the waves, the air boundary above the waves, and the waves themselves are in a complex nonlinear relationship. Their interaction is such that the wind-wave frequency spectrum, when $\omega > \omega_p$, depends only on u_*.

Swell is formally defined as old wind sea that has been generated elsewhere. Having come from elsewhere, bearing the imprint of a different storm, swell may propagate at any speed relative to the wind or at any angle to the wind. This property may be used to separate swell from actively growing wind sea in many cases. Since frequency dispersion can separate the components of swell as they propagate away from the source area, swell tends to have a narrower spectrum than wind sea, although its bandwidth may have considerable variation. Donelan et al. (1993) suggest considering two clearly defined cases of swell: (1) a distinct peak in the spectrum having peak phase speed greater than the wind component in the direction of propagation of the peak and (2) a distinct

peak in the spectrum having peak phase velocity at an angle greater than 90 degrees to the wind.

A general climatology of the wind sea and swell is given by Hanley et al. (2010) and is summarized here. Figure 2 shows an illustration of wind regimes separated based on the inverse wave age, defined as $\left(U_{10}\cos\theta\right)/c_p$, based on which the sea state climatology was categorized. Wind waves have large inverse wave age, greater than 1/12 (~0.83) when the waves are fully developed and reach a point of equilibrium with the winds (Pierson and Moskowitz 1964). The wind sea regime, as described earlier, is characterized by wind-driven waves when local atmospheric flow generates capillary waves (surface tension as restoring force) initially, and hence denoted as wind-driven regime in Figure 2. The wind waves usually have periods shorter than 15 s (Massel 1996). In the case of pure wind-waves, there is a strong correlation between wind and wave direction, resulting in small θ in the inverse wave age.

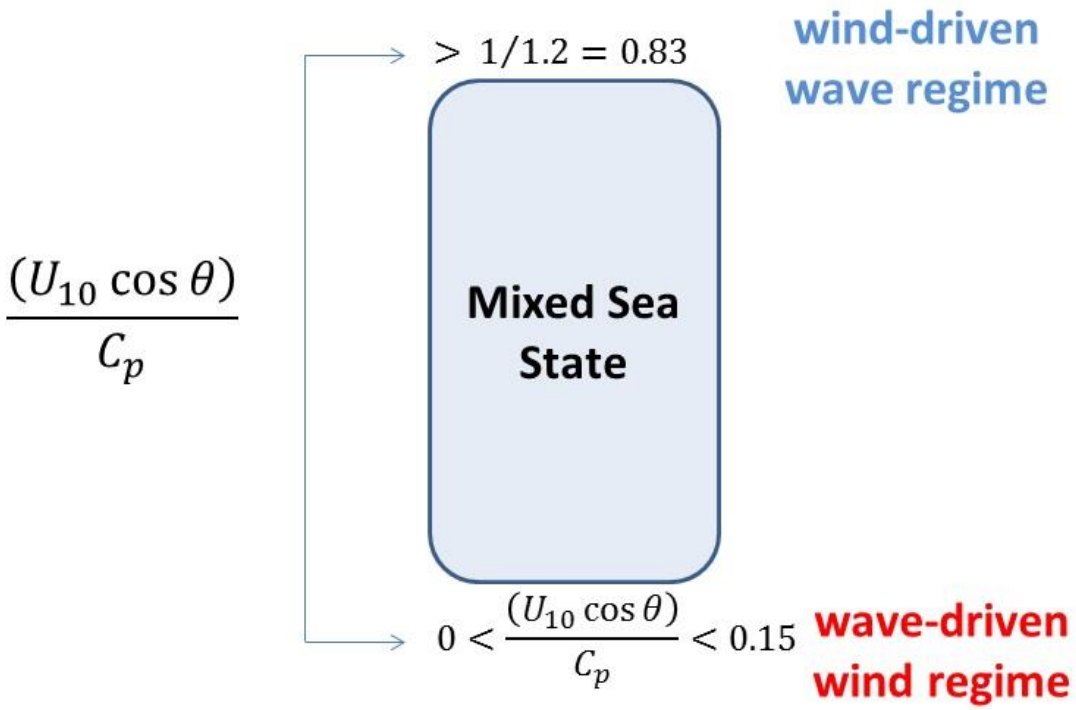

Figure 2. Wind-wave regime using inverse age parameter (after Hanley et al. 2010).

Henley et al. (2010), using analysis of wind and waves for a period from 1958 to 2001, found that the wind-driven waves are frequently seen in the Southern Ocean (more than 15%), in the Northern Hemisphere storm tracks (more than 10%), and also in enclosed seas and lakes due to fetch limitation.

For swell (wave-driven wind regime), the inverse wave age falls between 0 and 0.15. These conditions are found after a significant atmospheric disturbance in a distant geographical area, where the long waves travel for hundreds or thousands of kilometers from the source of the surface disturbance. Swell normally has a period longer than 15 s. The restoring force for swell is also the gravity force. Grachev and Fairall (2001) found a shift of the air-sea momentum flux from positive to negative values when the inverse age parameter drops below 0.15, which was an indication that the momentum transfer is from waves to wind. For this reason, this regime is also termed the wave-driven wind regime.

According to the climatology study by Hanley et al. (2010), swells are more common but not confined to the Tropical and Sub-tropical regions of the Southern Hemisphere (Pacific, Atlantic, and Indian Oceans). They are even more prominent on the eastern boundaries of the three ocean basins. Off Indonesia, swells occur more than 40% of the time. Regimes of frequent occurrence of swell are referred to as ‘swell pools’ by Chen et al. (2002) using measurements obtained by satellite altimeters and scatterometer. A global view of the locations of swell pools is shown in Figure 3. The swell pool in coastal Indonesia is a result of the energy released by storms year round in the Southern Ocean, hitting the Indonesian coast from south southwest.

The most frequently observed cases were in the mixed sea regime with the presence of a combination of swell and wind waves, where the inverse wave age falls between 0.15 and 0.83. In this category, waves can arrive from different directions and sources, involving differences in locations and speeds. In fact, the real ocean, especially over the open ocean, pure wind sea or swell conditions are a rare occurrence. This rarity suggests the complicated momentum transport in

these conditions, where the directions of momentum transport likely varies with wave length and/or propagation direction.

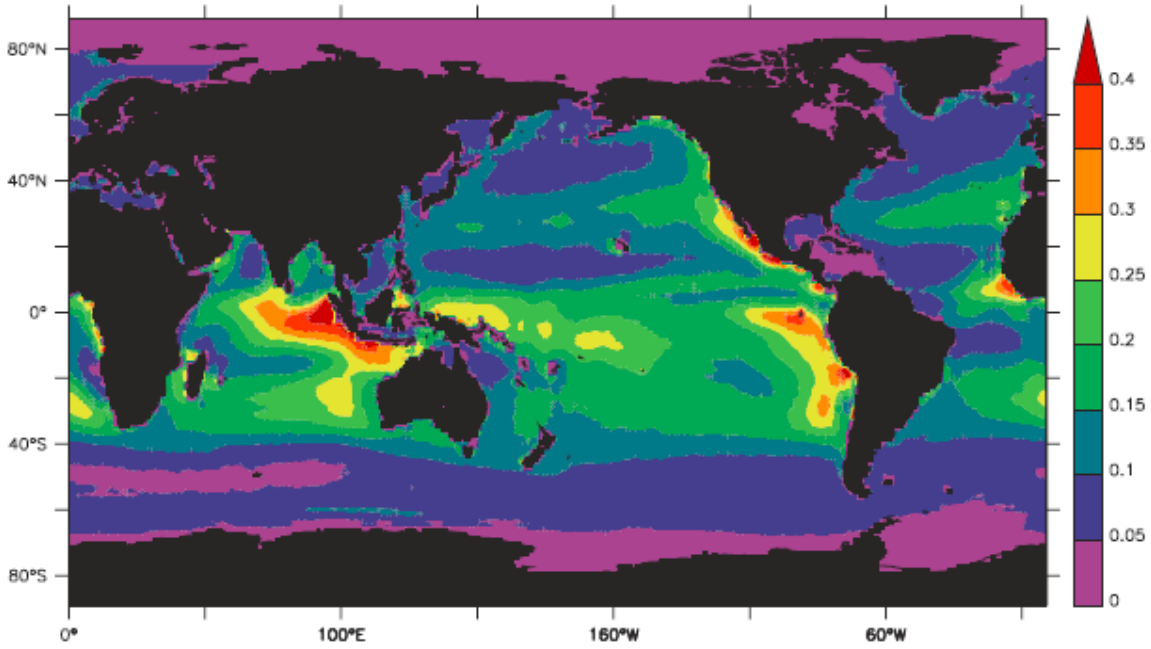

Figure 3. Swell pools obtained by Chen et al. (2002). Color bar represents the occurrence of swell.

C. WAVE EFFECTS ON SURFACE FLUXES

The sea surface is undulated by waves that are a mixture of swell and locally generated wind waves. The complexity of the sea surface undulation strongly depends on the interaction between wind and waves that is accomplished by wind-wave momentum exchange. Therefore, air-sea momentum flux is dependent on sea state. Since the wave disturbances transform the vertical structure of the atmospheric surface layer, sensible and latent heat, and gas exchanges should also be affected by the sea state, which in turn alters the momentum and energy transfer to waves. Hence, the evolution of and the atmospheric surface layer over wave surfaces have to be considered within the framework of coupled wind-wave interaction.

The impact of sea-state dependent surface flux representation on forecasting of synoptic disturbances has been studied in the past. For example, Doyle (1995) used the U.S. Navy's Coupled Ocean Atmospheric Mesoscale Prediction System (COAMPS) in conjunction with WAM (Wave Modeling) for a case study to simulate the evolution of a single depression. In this study, the Charnock parameter (to be discussed in the following paragraphs) was set to be a function of the surface stress from waves. His results suggested a surface sensible heat flux increase of 20% in the coupled simulation compared to the uncoupled simulation when the Charnock parameter α_c was set to be a constant. The sea-state dependent simulation also made significant difference to the evolution of the low pressure system as the rainfall maximum increased by 34%.

A relation between wind stress and sea state is also of considerable interest from a remote sensing viewpoint; it is not the wind itself but the wind-driven waves that determine the microwave signature of the surface. It is of crucial importance in the numerical modeling of wind wave growth (Perrie and Toulany 1990) and in the development of coupled models of surface wind and wave fields (de las Heras and Janssen 1992).

Since C_D has a one-to-one correspondence with surface roughness, z_0, for neutral stratification (Equation 2.3), z_0 has often been used instead of C_D in previous studies. Charnock (1955) obtained a relationship from dimensional analysis:

$$z_0 = \alpha_c \frac{u_*^2}{g} \tag{0.5}$$

where α_c is a constant called Charnock parameter (or non-dimensional roughness length), u_* is frictional velocity, and g is the gravitational acceleration. Since the wave field is generally larger at higher wind speed and results in higher momentum flux, the Charnock equation has an implicit dependence on the wave field.

Measurements over the oceans and lakes have shown a wide range of α_c. It is now well established that the drag coefficient (or equivalently the aerodynamic roughness z_0) and other surface fluxes are clearly impacted by the sea state as numerous researchers have found that stress is greater over the young and developing wave field than over an older wave field (Donelan 1990; Fairall et al. 1990). It has also been shown that z_0 variations are more profound at shallower sites (e.g., Geernaert et al. 1986, 1987; Smith et al. 1992) where there are frequent presences of young waves. Hence α_c varies significantly for young and developing waves. In fact, Volkov (1968) summarized all variables involved for describing predominate waves and dynamic characteristics of the neutral stability atmospheric surface layer. Based on the dependence of these variables on each other, he concluded that the number of variables needed to specify the problem of momentum transfer over waves surfaces into four variables: c_p, u_*, z_0, and θ, which are the phase velocity at the peak of the wave slope spectrum, the surface layer frictional velocity, the surface roughness, and the difference between wave and wind directions, respectively. The dependence of z_0 on wave age was proposed in an early study by Stewart (1974) on the basis of 'similarity' (i.e., by arguing that all purely wind-driven wave spectra should have similar shape) that the wave roughness of the sea surface should be mainly a function of the phase speed c_p of wind-waves at the spectral peak frequency. It follows by a dimensional argument that a general form of the wave-dependent non-dimensional roughness length, z_0^*, can be expressed as a function of the wave age c_p/u_*, a parameter discussed in the previous section to represent the state of growth of wind waves relative to local wind speed.

$$z_0^* = \frac{gz_0}{u_*^2} = f\left(\frac{c_p}{u_*}\right) \tag{0.6}$$

Equation (2.6) can be rewritten as:

$$z_0 = \frac{u_*^2}{g} f\left(\frac{c_p}{u_*}\right) \tag{0.7}$$

Equation (2.7) is essentially a modification to the Charnock equation (Equation 2.5) to include the sea-state parameters explicitly in surface flux parameterization.

The exact dependence of surface roughness on wave age, as is generalized in Equation 2.7, is not straightforward from measurements. Data collected over the ocean to date have shown fairly large scatter. Some of the scatter has to do with measurement error; some have to do with various factors of the wave conditions such as effects of the water depth, unsteadiness of the wind field, and the inherent assumption related to the constant flux layer or the log-wind profile assumption.

Since the short waves mainly contribute to the aerodynamic drag over the ocean, it may be argued that surface stress depends on the steepness of the short waves, which to a good approximation is given by the mean square slope. This parameter, however, is not straightforward to measure. The majority of previous studies still use wave age as defined earlier.

The effect of swell on the near surface wind profile is likely to be more pronounced in low-wind conditions. Conceptually, the effect is related to the direction of the wind and the direction of the swell, the two categories observed in the past as being wind following swell and wind opposing swell (Donelan et al. 1997). Because swell has a large phase speed, larger than the mean wind speed in low wind conditions, it is conceivable that momentum is transferred from the wave to the atmosphere when swell is running ahead of the wind, and the wind sea's contribution to roughness is minimal. Figure 4 provides clear evidence for an upward momentum transfer (Holland et al. 1981, reproduced in Figure 5.7 in Kraus and Businger 1994). The wind reversal at the lower levels, seen in Figure 4 during the periods of calm wind, was also observed by an earlier version of MASFlux (formerly MOAS) documented by Cheney (2011). Generally, the

addition of swell to a locally wind-generated sea alters the roughness of the surface in two distinctly different ways: (1) the swell contributes directly to the surface roughness, and the importance of this contribution depends sensitively on the direction of propagation of the swell relative to the local wind; (2) the swell attenuates the wind sea and, although the mechanism of attenuation is poorly understood, it may be expected to depend on the steepness of the swell and its propagation direction relative to that of the wind sea components. Because swells propagate over large distances, they are not strongly correlated with local wind forcing. Hence over the open sea where mixed sea states are frequently occurring, a simple relationship described in Equation 2.7 may not exist (Yelland and Taylor 1996). In addition, any attempt to predict the effect of swell on the drag will require detailed information on the directional properties of both wind sea and swell. Consequently, measurements at sea of the wind stress without concomitant information on the wave directional properties will exhibit considerable noise, much of which may be caused by the direction of swell propagation relative to wind direction.

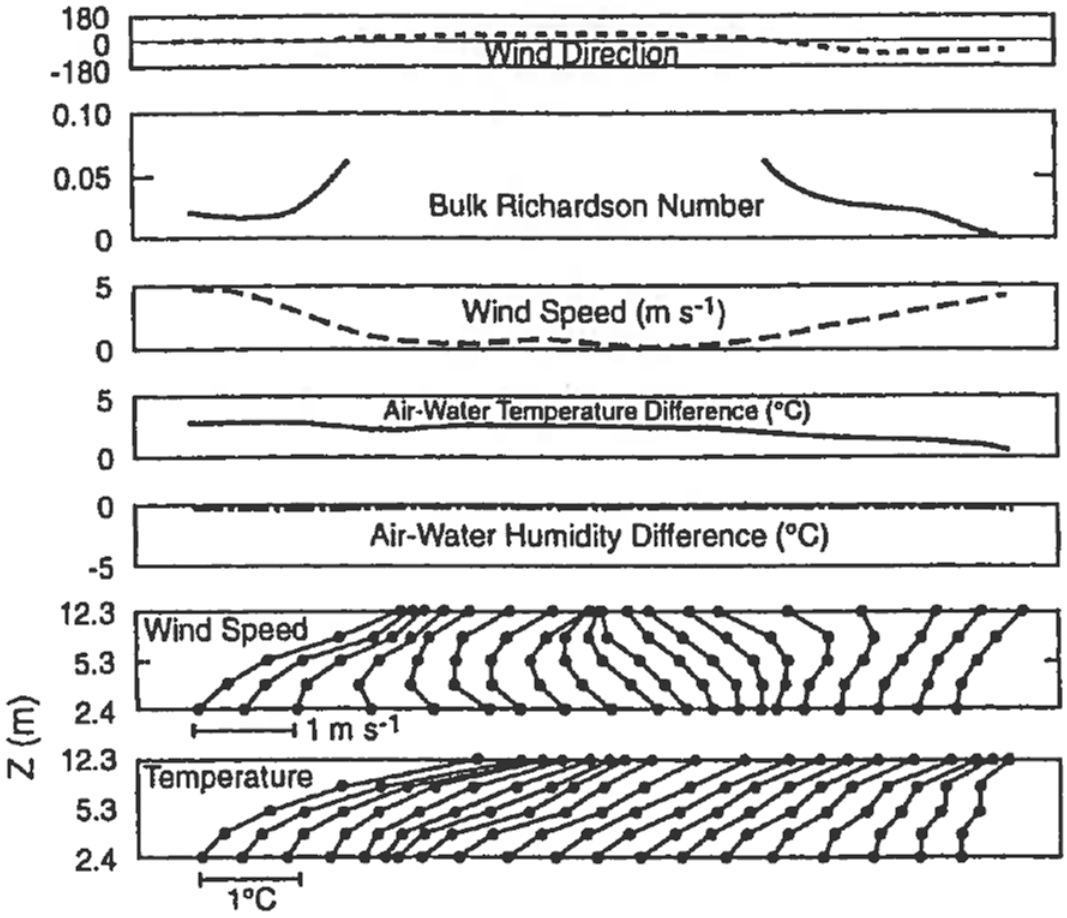

Figure 4. Upward momentum transfer (from Holland et al. 1981, reproduced in Figure 5.7 in Kraus and Businger 1994).

D. FLUX BUOYS FOR AIR-SEA-WAVE INTERACTION STUDY

It is seen in Equations 2.3 and 2.7 that the neutral drag coefficient C_{DN} and surface roughness length z_0 are related exponentially, and the inclusion of the wave age in surface flux parameterization is through Charnock's 'constant.' To investigate this complicated relationship, it presents very high demands on the measurement accuracy of U_{10} and u_*. Wind speed and friction velocity are normally measured in the vicinity of large bodies such as measurement platforms and ships. The presence of such large bodies inevitably leads to flow distortion. Consequently, corrections are needed for flow direction, wind speed, and friction velocity (for momentum). This is an inherent issue with ship-based

measurements (Yelland and Taylor 1996; Eymard et al. 1999) where the corrections are of considerable magnitude and are difficult to obtain. Well exposed anemometer measurements are hence preferred (Donelan 1982; Smith et al. 1992).

It should also be mentioned that the roughness over the oceans is very small ($z_0 \sim$ 0.1 mm) compared with that over land ($z_0 \sim$ 10 cm). The surface layer over the ocean is also often very thin; therefore, measurements at a fixed height may not give the surface layer fluxes when the surface is below the measurement height. Donelan (1990) found that the measured stress at an observation height of 10 m introduces a systematic underestimation of the surface stress. Such deviation of the measured stress from the surface stress is wind speed-dependent and may exceed 30% for some cases. Also of note is that the most direct measurement of surface stress is the eddy correlation method. The inertial dissipation method, used frequently in the past, involves assumptions of classical Monin-Obukhov similarity and may be valid in some conditions such as swell dominant cases (Drennan et al. 1999). In addition, Janssen (1999) suggested that the developing waves may modify the surface layer dynamics through pressure-velocity correlation and thus increase the surface stress, a factor not considered in MOST.

Because of the issues discussed in the preceding paragraphs, it is not surprising that results in the sea-state dependence of surface flux have shown large scatterings. From a measurement point of view, the preferred measurement setting is from a small platform and with high-rate sampling of the turbulent perturbations. Buoy-based measurements with flux sampling capabilities are most ideal. In fact, measuring ocean waves and surface temperature and atmospheric mean and momentum stress from instrumented buoys has been carried out for many years with great success. Existing buoys with these measurement capabilities are introduced in the following sub-sections.

1. Air-Sea Interaction Spar (ASIS) Buoys

The ASIS buoy is a stable platform and has low flow disturbance characteristics in both atmospheric and oceanic surface boundary layers. It was intended to be capable of reliably and accurately measuring directional wave spectra, atmospheric surface fluxes, and radiation in the open ocean and over coastal waters with minimal corrections.

The ASIS buoy has a unique design consisting of several spar members along the perimeter of an open cage. This design allows the buoy to have a mechanical response that reduces the motion of sensors relative to the surface, while retaining the low flow disturbance characteristics of a slender spar. Compared to other flux buoys, ASIS buoys have provided a significant improvement in current observational capability for interfacial and near-interfacial measurements.

ASIS is superior over other flux sampling buoys in its wave measurements. Owing to its unique configurations of capacitance wires, it can sample much smaller waves with better resolution, allowing detection of waves with significant wave height (SWH) up to 0.1 m. It can also be used in both a drifting or tethered mode. When tethered, it is attached to a moored tether buoy that itself can be used to deploy sensors over the full water column and to provide additional power and data storage capacity. Graber et al. (2000) gives a full description of its design and measurements characteristics. The upper portion of the ASIS buoy is shown in Figure 5.

The ASIS buoy is roughly 15 m of height and 280 lb in weight. Due to its modular construction, it can be disassembled to fit inside a 20 ft shipping container. Although this is a significant improvement over other flux sampling buoys, its size and weight still require a sizable vessel for on-site assembly and deployment.

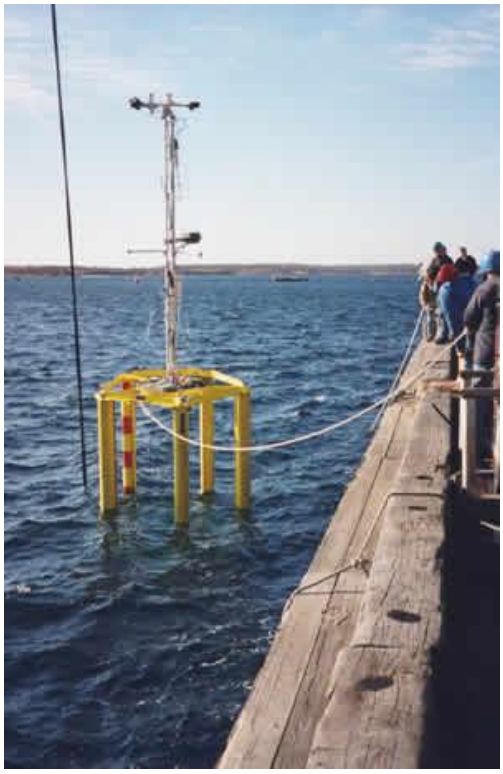

Figure 5. ASIS buoy during dock test.

2. NPS Flux Buoy (FB)

The Meteorology Department of NPS developed a flux buoy to provide direct measurement of air-sea fluxes, mean meteorological and oceanographic parameters, and surface wave characteristics (Frederickson and Davidson 2003). The measured parameters include wind speed and direction, air and sea temperatures, relative humidity and atmospheric pressure, as well as surface wave conditions. This platform allows measurements of those factors with very little flow distortion and thermal contamination compared to those from research vessels with carefully calibrated and maintained sensors, providing necessary near-surface quantities to air-sea interaction study as well as for applications related to electromagnetic wave propagation.

The FB is approximately 4 m above the waterline with a buoy hull 2 m in diameter and weighs 1,100 kg. Apparently, the size of this buoy does not allow

for deployment from a small boat. The reader is referred to Frederickson and Davidson (2003) for details on the NPS FB.

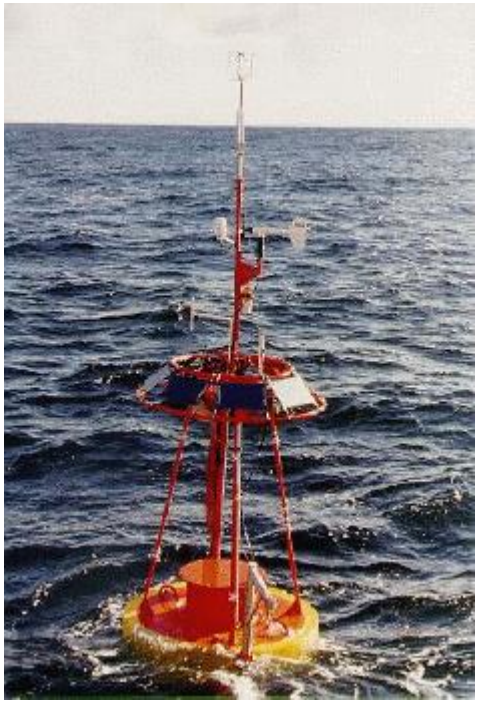

Figure 6. Deployed FB.

3. Woods Hole Flux Buoy

A recent addition to the flux buoys is the one developed at the Woods Hole Oceanographic Institute for long-term sampling of meteorological and oceanographic data over deep water close to 5 km in depth with strong currents and sea states. A surface mooring (3-m-diameter disc buoy) provided the platform on which to mount meteorological sensors and associated data-logging and telemetry hardware. The objectives for developing this buoy included obtaining measurements to describe the surface meteorology and to estimate the air–sea fluxes of heat, freshwater, and momentum by bulk formula methods (Fairall et al. 1996) with redundant, calibrated meteorological sensors, as well as having a direct covariance flux system (DCFS; Edson et al. 1998) for direct estimates of air–sea momentum and sensible heat fluxes. This buoy is also

designed to obtain upper-ocean currents, temperatures, and salinities. Unique from other flux buoys, the Woods Hole flux buoy samples the lower level in the atmosphere (up to 3.6 m above the sea level) with redundant sensors, and oceanographic variables in 20 levels, from almost the surface (0.89 m) to down below 600 m. A schematic diagram of the surface mooring is shown in Figure 7.

The surface mooring was deployed continuously for 15 months, beginning in November 2005, at 550 km from the coast of Massachusetts for long-term measurement of the Gulf Stream, which provided unprecedented data with significant climate impact, particularly for this region (Bigorre et al. 2012).

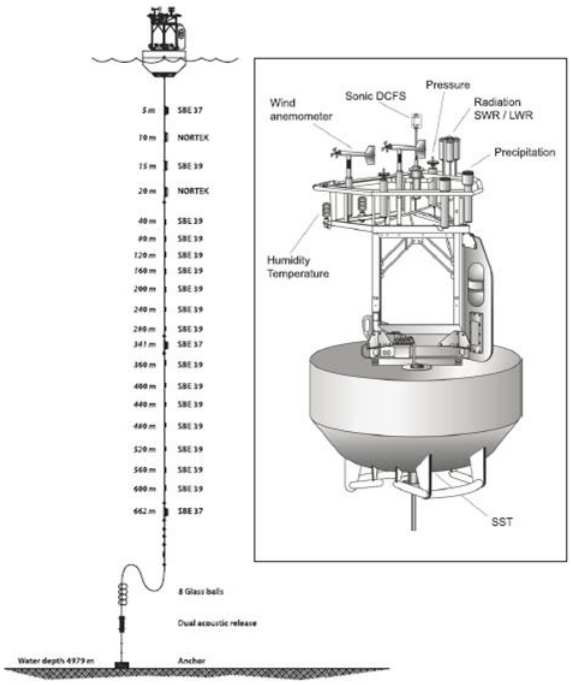

Figure 7. Schematic diagram of the surface mooring developed by the Woods Hole group (from Weller et al. 2012).

4. Other Flux Measurement Platforms

The Floating Instrument Platform (FLIP) has been an extremely important platform for air-sea interaction study since early 1960s (Fisher and Spiess 1963). It was designed to be a stable platform for mounting various types of near-

surface measurements. The 355-ft-long craft transits in horizontal position and operates in vertical position to obtain oceanographic and meteorological data.

A recent development in flux sampling buoys is the extreme air-sea interaction (EASI) buoy involving a 6 m NOMAD buoy by the same group at the University of Miami who developed the ASIS buoy. This new system was designed to complement the ASIS buoy to allow a wider range of experimental designs and high-resolution marine flux, directional wave, and turbulence measurements in extreme weather conditions such as those experienced in typhoons. The EASI buoy and the ASIS buoy were deployed in tandem in the typhoon-prone western Pacific Ocean in 2010, providing concurrent and co-located measurements of the near-surface dynamics in both the Marine atmospheric boundary layer (MABL) and Oceanic boundary layer (OBL) (http://www.rsmas.miami.edu/news-events/press-releases/2011/the-buoys-are-back-in-town). In addition to sampling under extreme conditions, an area with significant data void, the EASI buoy also allows estimates of spray and foam from breaking waves and how they affect the drag coefficient in typhoon force winds, another area that has no reliable direct measurements in extreme conditions.

III. MASFLUX SYSTEM CONFIGURATION AND TEST DEPLOYMENTS

MASFlux is developed based on earlier efforts of NPS in developing a small buoy for air-sea interaction study which resulted in MOAS, as described by Cheney (2011). MOAS used the same buoy float and was configured to measure the near surface profiles of temperature, humidity, and wind speed as well as the sea temperature in the upper 0.5 m of the ocean. The uniqueness of MASFlux and MOAS is their small size and light weight. These qualities make them easily deployable with two to three people and allow for measurements to be carried out using a small boat. Having a small platform, MASFlux also avoids one of the major difficulties in obtaining measurements near the air-sea interface, which is the flow and heat distortion caused by the measurement system itself (Edson et al. 1998). In this chapter the MASFlux configuration and instrumentation are described (in sections A and B, respectively) along with descriptions of the test deployment in the Monterey Bay (section C).

A. MASFLUX CONFIGURATION

Since the first test, MASFlux has been continuously modified with minor adjustments until its final configuration (Figure 8) in the test deployment on December 7, 2012. A major addition to MASFlux occurred after the deployment on November 2, when a compass was added to the system. This compass, which provides magnetic heading, replaced the low-quality heading measurements from the accelerometer identified during the initial data analyses of the previous MASFlux deployments. Both sea and atmospheric temperature, wind, and humidity sensors were kept at the same levels since the first test deployment.

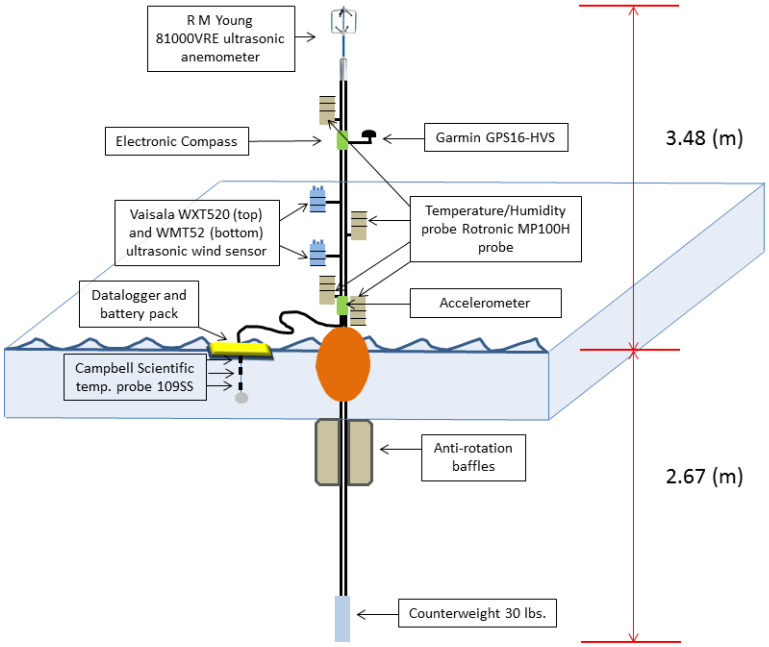

Figure 8. MASFlux sensor configuration.

Overall, the buoy is composed of a mast of approximately 6 m long (20 ft) supported by a Scanmarin inflatable spar buoy (MR60) with 61 kg (134 lb) of flotation capacity. There are four levels of temperature and relative humidity sensors within the lowest 3.5 m of the atmosphere. Vaisala combined weather sensors are set at two levels, providing wind speed and direction measurements. Near surface atmospheric pressure was also available in later deployments. An ultrasonic anemometer is used to obtain atmospheric turbulence at high sampling frequency (20 Hz). Underwater temperature measurements were obtained using sea thermometers located at three different depths within the top 0.5 m of the water. The distances were selected to obtain sea temperature as close as possible to the immediate surface due to the large temperature variation within one meter depth (Kawai and Wada 2007). Hence, the top level measurements can be used in place of the sea surface temperature with minimum error.

In the order to identify the wave effect on the measurements and buoy motion and orientation for a more accurate flux measurement, a compass and an accelerometer were also installed on the buoy mast. All the sensors were

connected to a Campbell Scientific CR3000 datalogger as the data acquisition system for data collection and synchronization. Because of its small internal memory, a 2 Gb memory card was added allowing approximately 22 days of consecutive data collection. The sensors installed on the December 7 and later versions of the MASFlux are listed in Table 1. The corresponding variables from the sensor are also given.

Sensor	Height (m)	Measured variables
Ultrasonic Anemometer R M Young Model 81000VRE	3.48	High frequency wind speed and wind direction. Sonic temperature
Temperature and Humidity Probe Rotronic Model MP100H	3.07, 1.54, 0.77 and 0.38	Temperature Relative humidity
Vaisala Weather Transmitter WTX520	1.83	Wind speed and direction Barometric pressure
Vaisala Weather Transmitter WMT52	0.87	Wind speed and direction
Campbell Scientific Temperature Probe Model 109SS	-0.03, -0.16 and -0.41	Sea water temperature
Garmin GPS16-HVS	2.9	Position Velocity Magnetic declination
True North Revolution Technologies GS Gyro Stabilized Electronic Compass	2.9	Heading Pitch Roll
VectorNav VN-100 Rugged Accelerometer	0.6	Angular rates, linear accelerations Magnetic field components

Table 1. MASFlux sensors setup.

In previous configurations of this spar buoy, the batteries and datalogger were mounted onto the pole, increasing its weight by 8 kg and affecting its stability. The current version has the datalogger and the battery pack enclosed within a Pelican case Model 1400NF, which has a buoyancy maximum of approximately 9 kg. Cables from the sensors are routed to the mast by an umbilical arrangement. The length of the cables is long enough to prevent tangling and also minimizes drag and tilt of the spar buoy.

After the first deployment, the radar reflector was removed due to possible perturbation in the collected data and its effect on pole stability, even in light wind conditions. The reflector was located between the ultrasonic anemometer and the first (highest) Temperature/Humidity probe.

B. MASFLUX INSTRUMENTATION

Sensors installed in the MASFlux are mentioned in this section. Detailed features of meteorological, oceanographic and GPS sensors are presented in Table 2, and those of the accelerometer and compass in Table 3.

Ultrasonic Anemometer R M Young Model 81000VRE				
Parameter	Wind speed	Wind direction	Sound speed	Temperature
Range	0 to 40 (ms^{-1})	0 to 360 (deg)	300 to 360 (ms^{-1})	-50 to +50 (˚C)
Resolution	0.01 (ms^{-1})	0.1 (deg)	0.01 (ms^{-1})	± 2 (˚C) from 0 to 30 (ms^{-1}).
Accuracy	±1% ±0.05 (ms^{-1})	± 2 (deg) at 30 (ms^{-1}). ± 5 (deg) at 40 (ms^{-1})	0.1% ± 0.05 (ms^{-1}) at 30 (ms^{-1})	
Other	Threshold: 0.01 (ms^{-1})	Elevation range: ± 60 (deg)		

Temperature/Humidity Probe Rotronic model MP100H		
Parameter	Temperature	Humidity
Range	-40 to +60 (˚C)	0 to 100 (%RH)
Accuracy at 23 (˚C):	Pt100: ± 0.03 (˚K)	± 1.5 (%RH)
	HygroClip: ± 0.3 (˚K)	

Vaisala Weather Transmitter WTX520 and WMT52			
Parameter	Wind speed	Wind direction	Pressure
Range	0 to 60 (ms^{-1})	0 to 360 (deg)	600 to 1100 (hPa)
Resolution	0.1 (ms^{-1})	1 (deg)	0.1 (hPa)
Accuracy	±3% at 10 (ms^{-1})	± 3 (deg)	± 0.5 (hPa) at 0 to +30 (˚C) ± 1 (hPa) at -52 to +60 (˚C)

Campbell Scientific Temperature Probe Model 109SS		Garmin GPS16-HVS	
Temp. range	-40 to +70 (˚C)	Position:	3 meters
Temp. accuracy	± 0.49 at -20 to +70 (˚C)	Velocity:	0.1 RMS steady state.
Submersion depth	150 ft (63 psi)	PPS:	± 1 (µs)

Table 2. Meteorological, oceanographic and GPS sensor specifications.

True North Technologies Revolution GS Gyro Stabilized Electronic Compass			
Heading		Pitch and roll	
Accuracy	± 3.0 (deg) RMS at dynamic, rate < 150(deg s^{-1})	Accuracy	± 0.2 (deg)

Response time	36 (msec)		Repeatability	± 0.2 (deg)	
Dip angle	± 80 (deg)		Range	± 40 (deg)	
Tilt range:	± 40 (deg)				
VectorNav VN-100 Rugged Accelerometer					
Parameter	Attitude & Heading	Angular Rate	Acceleration	Magnetic field	Pressure
Range	Heading, roll: ± 180 (deg) Pitch: ± 90 (deg)	± 500 (deg s^{-1})	± 8 (g)	± 2.5 (Gauss)	10 to 1200 (mbar)
Linearity		< 0.1 % (FS)	< 0.5 % (FS)	< 0.1 %	
Accuracy	Static heading: < 2.0 (deg) Static pitch, roll: < 0.5 (deg)	Alignment error: ± 0.05 (deg)	Alignment error: ± 0.05 (deg)	Alignment error: ± 0.05 (deg)	± 1.5 (mbar)
Resolution	Angular: < 0.05 (deg)				0.042 (mbar)

Table 3. Accelerometer and compass specifications.

1. Ultrasonic Anemometer R M Young Model 81000VRE

Located on the top of the mast at 3.48 (m), this sensor is vital for obtaining flux information. It is the most important upgrade to the buoy used by Cheney (2011). It provides three dimensional wind velocity and speed of sound from the transducer array. Data are collected at a frequency of 20 Hz, the rate needed for obtaining flux from the eddy covariance method (Burba and Anderson 2010). It measures the vertical and horizontal wind velocities which are used for calculating turbulent statistics after removal of the platform movements. This process is made using the fast data sampling collected by the accelerometer (IMU) and compass.

2. Temperature/Humidity Probe Rotronic Model MP100H

In the design of MASFlux, there are four of these sensors, located at 3.07, 1.54, 0.77 and 0.38 m above the sea level, providing measurements of temperature and relative humidity. The mounting heights were chosen considering a logarithmic scale. The probe by itself has a sensor called

HygroClipS3, which is used to measure the relative humidity, and temperature is sampled with an external Pt100 sensor. Sensors were installed in a multi-plate radiation shield, R M Young model 41003, to reduce errors caused by solar radiation and precipitation. Data were collected at 1 Hz.

3. Vaisala Weather Transmitter WXT520 and WMT52

These two-dimensional wind sensors were used to obtain wind speed and direction. The initial configuration of MASFlux was designed with a WXT520 sensor installed at 1.83 and a WMT52 in the lower level at 0.87 meters above the sea level. During October and November deployments, the WXT520 was used at both levels. The last three deployments were the same as the first deployment, shown in Figure 8. Both sensors have the same range, resolution and accuracy in terms of wind measurements. The WMT52 measures wind only. Data were collected at 1 Hz.

4. Campbell Scientific Temperature Probe Model 109SS

These probes were used to obtain sea water temperatures at three different depths (3, 16 and 41 cm). Thermometers were suspended from the umbilical cable using a separate small float and a weight. Depths were selected within the first 50 cm of the water column for the purpose of obtaining values close to the thermal skin layer.

5. Garmin GPS16-HVS

This sensor was installed primarily to track horizontal displacement (drift speed and direction) and to correct two-dimensional winds measurements. Also the GPS reports the magnetic declination globally, so the electronic compass can be corrected to true north. Due to its waterproof property, it is ideal for maritime measurement. It has 12 different reception channels, allowing the GPS to track up to 12 satellites obtaining one-second navigation updates.

6. True North Technologies Revolution GS Gyro Stabilized Electronic Compass

This compass is designed for rough movement platforms, such as the ones in marine conditions. It was added after the November deployment due to the uncertainty in heading data from the accelerometer. It was set at 5 Hz acquisition rate for heading, pitch and roll. The location of this new sensor was at the same height of the GPS antenna, mounted within a small splash-proof case.

7. VectorNav VN-100 Rugged Accelerometer:

This sensor was positioned in a small box between the two lowest Rotronic sensors, at 0.6 m above sea level. The outputs recorded were three component linear accelerations, three rotational accelerations, and after the November deployment, three components of the magnetic field. During post-processing, it was determined that yaw was not reliable. The sampling rate was set at 20 Hz, the same frequency used for the 3-D Ultrasonic anemometer.

C. MASFLUX FIELD DEPLOYMENT AND DATA QUALITY

The MASFlux was tested in the Monterey Bay in six deployments during the period between August 2012 and May 2013. Based on the sensors and the buoy configuration, the test deployments are described below in two groups as Stages I and II, respectively. The major difference between the two stages is the addition of a gyro stabilized electronic compass in the December 7, 2012, deployment. Other minor changes will be noted in the deployment descriptions that follow. Measurements from deployments in Stage II are analyzed as part of this research. Four cruises were on board of the National Oceanic and Atmospheric Administration (NOAA) craft R4107, and two were on the NOAA R/V Fulmar. The locations of all test deployments (except for the August 2012 deployment) are shown in Figure 9, together with available buoy stations in the Monterey Bay area.

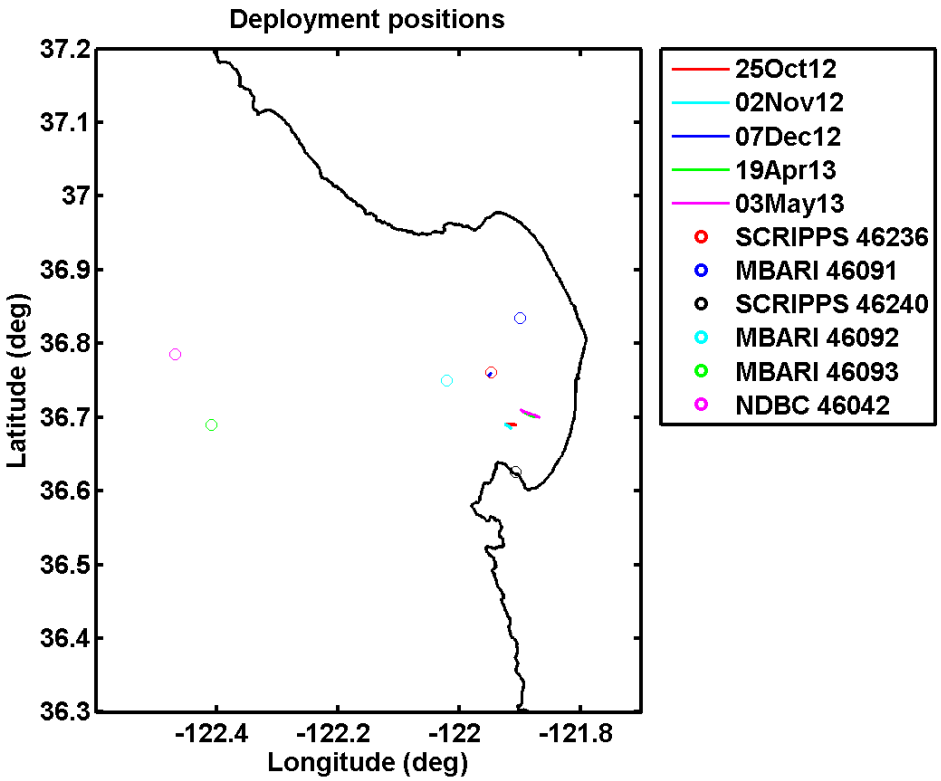

Figure 9. MASFlux test deployments in the Monterey Bay and location of buoys for meteorology and/or wave and upper ocean measurements in the area.

Before the first at-sea deployment, the instrumented buoy was float-tested from the dock at Moss Landing, CA in light wind and calm sea conditions. See Figure 10 for a view of the buoy, which rode well, at dock testing.

Figure 10. MASFlux in the floatation and stability test.

The majority of the at-sea tests were conducted on board the NOAA craft R4107 (Figure 11). This vessel is intended to support the management of the Monterey Bay Marine Sanctuary and to provide a safe working platform for research and educational operations. The catamaran's dimensions are 41 ft in length and 14 ft of beam, with 4 ft of draft. It has a diesel/biodiesel propulsion system with a maximum speed of 28 kn and an operating range of 300 nm. The capacity for day trips is ten people (including two crew and researchers/students), and for overnight operations the number is reduced to four.

The vessel used for the last two cruises was the 67-ft R/V Fulmar, also owned and operated by NOAA. On both vessels, the 6-m long MASFlux buoy was attached to the handrail during transits to the deployment sites.

Figure 11. NOAA R4107 used for MASFlux deployments over the Monterey Bay.

1. Stage I: Deployments without Gyro Stabilized Electronic Compass (August–November 2012).

Four cruises were made in the initial stage of buoy testing. As was mentioned before, this stage consisted of four deployments; all of them were on board the NOAA R4107. Although the data and results from these deployments are not shown in this thesis, the buoy settings and environmental conditions are described briefly here to provide a record of the evolution of the buoy system in each successive deployment.

a. August 22, 2012

This cruise was made under light wind conditions and SWH of ~1 m with period of 7 s. A Datawell Directional Waverider buoy (DWR-G4) was also deployed allowing comparison of wave measurements by the MASFlux. Data

were collected in two periods of approximately 50 min each. Data collection was successful in terms of a functionality test, although it was discovered that one of the WMT52 wind sensors' measurements were problematic. Despite the light wind conditions, the buoy tended to tilt and rotate because of the effect of the radar reflector. As a result, data from this deployment is not going to be considered in the final discussion of the results in this thesis.

b. October 25, 2012

During this deployment, swell dominated the ocean surface waves with approximately 1 m SWH and a period of 9.88 s based on the measurements from the closest National Data Buoy Center (NDBC) station (46236). Data were collected for approximately 100 m. It was noticed during the deployment that the buoy had a pronounced rotation, which appeared to be caused by the drag of the mounted sensors fighting the pull of the umbilical cable. This deployment also included a DWR-G4 wave buoy.

The main changes from the first deployment to the second one included adding an external memory card of 2 GB to the datalogger to allow 22 days of storage, changing the sampling rate of the GPS to update to every second, and replacing the malfunctioning WMT52 wind sensor at the 1.83 m level with a similar sensor (WTX520), and adding barometric pressure measurements to the MASFlux system. In addition, the radar reflector was removed from the mast in an effort to reduce the wind-induced tilt of the mast.

c. November 2, 2012

Similar to previous deployments, the MASFlux was deployed from the NOAA R4107 along with a DWR-G4 wave buoy from the NPS Oceanography Department. The only change made for this deployment was to modify the below-waterline rudder by adding a second panel and orienting the two rudders to form a cross shape. This modification seemed to reduce the rotational oscillation problem, but the buoy still had noticeable motion. According to measurements from the NDBC station 46236, SWH was 1.4 m with a predominant period of 10

s, along with swell conditions less than 1 m wave height. Wind conditions were light to moderate during the deployment, generally weaker than 7 ms^{-1}.

2. Stage II: Deployments from December 7, 2012

a. December 7, 2012

Analyses of measurements from the October and November deployments revealed a drift in the heading output from the accelerometer on the MASFlux. As a result, a gyro stabilized electronic compass was added to the system, which was test deployed on December 7, 2012. This addition is essential to the MASFlux because a reliable heading is crucial for accurate flux measurements.

This deployment was made from the NOAA R4107 along with five different wave buoys from the NPS Oceanography Department. The nearby NDBC buoy showed that the SWH was consistent at 1.8 m with a peak period range between 9 and 11 s. Wind was light from NE changing to N at the end of the measurement period.

b. April 19, 2013

This deployment was carried out on the NOAA R/V Fulmar. The MASFlux was modified by raising the position of the anti-rotation rudders closer to the buoy float in hope of less rotational motion. Follow-up analyses of the data suggested that this modification indeed reduced the rotation of the buoy. However, this modification also reduced the buoy response to vertical displacement of the waves.

During the deployment, wind speeds varied between 2 and 9 ms^{-1} with a steady direction from the WNW. The significant wave height was reported to be around 1 m with a peak period around 8 s from the same direction as the wind. One DWR-G4 wave buoy was also deployed simultaneously with the MASFlux.

c. May 3, 2013

The MASFlux was tested again on May 3, 2013, using the same system configuration as on April 19 on the R/V Fulmar. The MASFlux and DWR-G4 wave buoy were deployed simultaneously at around 10:30 PDT and were retrieved after about three hours of continuous measurements.

Wind speeds were less than 3 ms^{-1} from the North during the first hour, increasing to 6 ms^{-1} for the rest of the deployment with a westerly component. The predominant waves were from WNW with a SWH of 1.4 m and period of 9 s.

IV. CHARACTERISTICS OF SURFACE FLUX, MEAN PROFILES, AND OCEAN WAVES FROM MASFLUX MEASUREMENTS

Results from the different components of the MASFlux, including ocean surface waves, atmospheric surface layer turbulence, low-level mean wind, temperature, and humidity at multiple levels, and mean water temperature near the surface at multiple levels, are presented in this chapter. The characteristics of each sensor are given in Chapter III. Measurements from the Stage I buoy deployment were mainly used to diagnose buoy motion and disposition issues and were used for the subsequent deployment. This chapter only presents results from Stage II buoy deployments for the MASFlux.

All slow-rate air and water temperature sensors for temperature profile measurements were calibrated to ensure that the differences seen in the measurements from different levels were not contaminated by the bias of individual sensors. The calibration procedure used a hot and cold bath method by submerging all temperature sensors in room temperature water for about 25 minutes. The temperature of the water was then adjusted to colder temperatures by adding ice to the tub. A mean temperature from all sensors were obtained for each time instant, and the deviations of each sensor from this mean is obtained. The time-averaged deviation of each sensor for both the hot and cold periods is the calibration for this sensor and would be removed from the measurements before the analyses. The maximum magnitude of the calibration adjustment was approximately 0.03^{o}C. Results from each calibration were found to be rather consistent. In addition, a sensor assigned for a certain level was reserved for that level for all deployments.

In section A, wave measurements from MASFlux are compared to those from the Datawell wave buoy deployed simultaneously in each deployment. Turbulence measurements are shown in section B with turbulent power and co-spectra compared to the expected power spectra in the inertial sub-range. The

measured mean profiles of temperature and wind are discussed in conjunction with the turbulence characteristics in the same section.

A. WAVE MEASUREMENT AND VALIDATION

Concurrent wave and flux measurements are crucial for the study of air-sea-wave interaction. The quality of wave measurements from the MASFlux is evaluated against those from the Datawell wave buoys in this section, where comparisons of wave energy and directional spectra are made. Also included in these comparisons are bulk parameters such as significant wave height (SWH), which is the average height (trough to crest) of the one-third highest wave, peak wave period (Tp), and its direction (DTp).

The Monterey Bay region represents complex spatial variability in the atmosphere and in the water. In general, waves propagating from deep water to shallow water regions experience substantial modification due to refraction, diffraction, shoaling and energy dissipation associated with bottom surface and topography. These non-linear effects are magnified in places like the Monterey Bay, which has a complex geometry of the coastline and significant gradient in bathymetry. The strong influence of the bathymetry is shown in the variation of the Rossby radius of deformation (Figure 12), which is around 10 km near the Monterey Canyon, reaching its lowest value 0.9 km in the southernmost point (Breaker and Broenkow 1989).

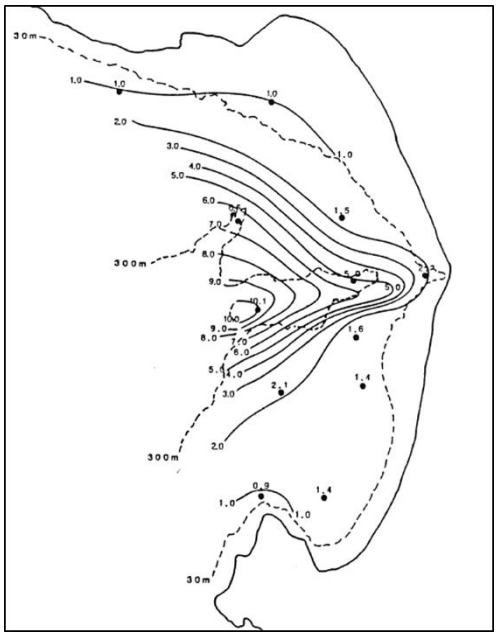

Figure 12. Rossby radius of deformation in the Monterey Bay (from Breaker and Broenkow 1989).

As a result of the strong spatial variability, it is important that the validation of wave measurements be made in the proximity of the MASFlux. For this reason, we do not use the existing buoy measurements in the Monterey Bay region (Figure 9), but rather use the Datawell buoys deployed at the same time as the MASFlux. The longest separation between the MASFlux and the Datawell buoy was ~100 m for the May deployment.

The DWR-G4 is an easy-to-use, hand-deployable buoy (40 cm diameter), which employs a GPS sensor to measure the horizontal and vertical velocities based on Doppler shift signal. After one month of co-located measurements, the performance of the DWR-G series buoys using GPS technology were evaluated by de Vries et al. (2003) against the traditional Datawell buoys using compass and accelerometers. De Vries et al. (2003) concluded that the new GPS DWR-G buoys are capable of producing as high quality wave measurements as the traditional compass/accelerometer wave buoys. Their findings validate the use of the DWR-G4 here to evaluate the MASFlux wave measurements.

For wave data processing, we used the measurements in 20-minute data segments to avoid non-stationary effects (Herbers et al. 2012). The wave spectral analyses scheme was developed by Dr. John Kalogiros (NPS contractor) based on methods described by the NDBC (NDBC 1996). The Direct Fourier Transform Method (DFTM) was used for wave energy analyses and directional spectra calculation. All spectra calculations used 256 points in each 20 m of data with a sampling rate of 1.28 Hz (DWR-G4 sample frequency, MASFlux data was subsampled into 1.28 Hz for the wave spectra analyses). Thus, the highest resolvable frequency is 0.64 Hz. De Vries et al. (2003) suggested that the Datawell buoy has a low frequency limit of 0.033 Hz. Hence, the valid spectra range for wave measurement comparison is between 0.033 and 0.64 Hz.

Low signal to noise ratio is a problem for low frequency waves. This high noise level in lower frequencies is attributed to small wave acceleration in low frequencies compared to the gravity waves and also to pitch and roll contaminations by higher-frequency waves (Pearman et al. 2013).

An example of the 2-D wave spectra from one 20-minute segment measured on May 3, 2013, is shown in Figure 13. The dominant energy in swell at about 0.1 Hz frequency from northwest direction is apparent in the figure. The much weaker higher frequency waves are seen from the same direction. This figure is typical of the measurements from the last three deployments as the wind from all cases was rather weak, resulting in weak wind seas.

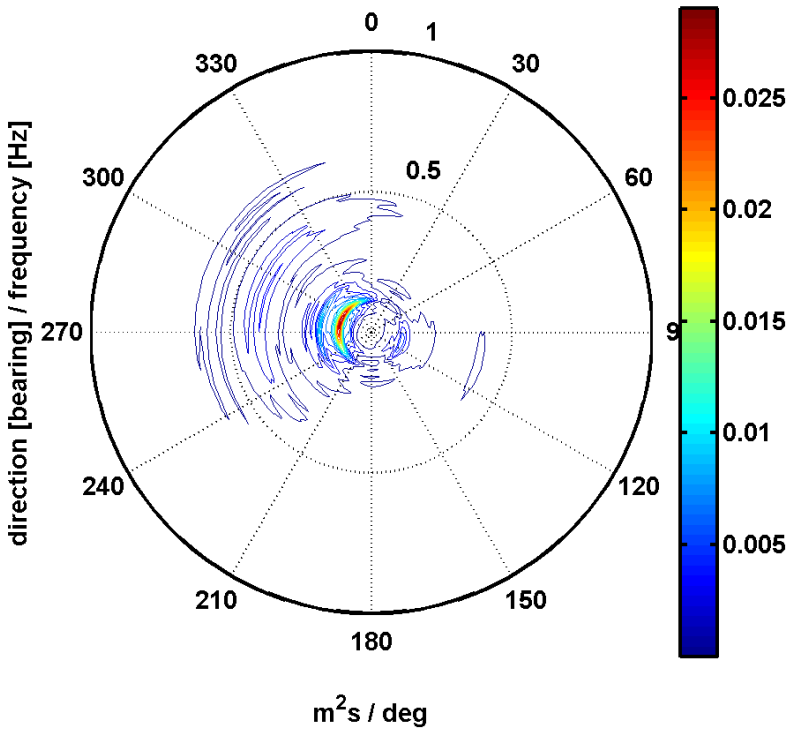

Figure 13. 2-D wave spectra from one 20-minute segment measured on May 3, 2013, deployment.

Comparison of the wave spectra between MASFlux and DWR G-4 was made for energy and directional spectra as well as wave statistics such as SWH, Tp and DTp.

The energy spectra from all three days, color-coded for different 20-minute data segments, are shown in Figure 14. It is clear that swell dominated the wave energy on all three days, with December 7, 2012, having the most significant swell and May 3, 2013, the weakest swell. The peak frequency is approximately 0.1 Hz for all cases. The peak frequencies from all data show very good agreement, with discrepancies of less than 0.01 Hz in frequencies. We also notice that, with the exception of May 3, 2013, the wave field from different 20-minute data segments on the same day are very similar, denoting that the wave field was rather stationary during the several hours of measurements. On May 3, 2013, the high frequency wind waves show an energy increase with time; the reason for this increase is not clear. However, this case shows us how well the

MASFlux wave measurements match those from the surface wave buoy. When plotted for comparison for each time segment only, one can see the MASFlux spectrum follows almost exactly the DWR-G4 spectrum for each segment, even though there are significant differences from one segment to another.

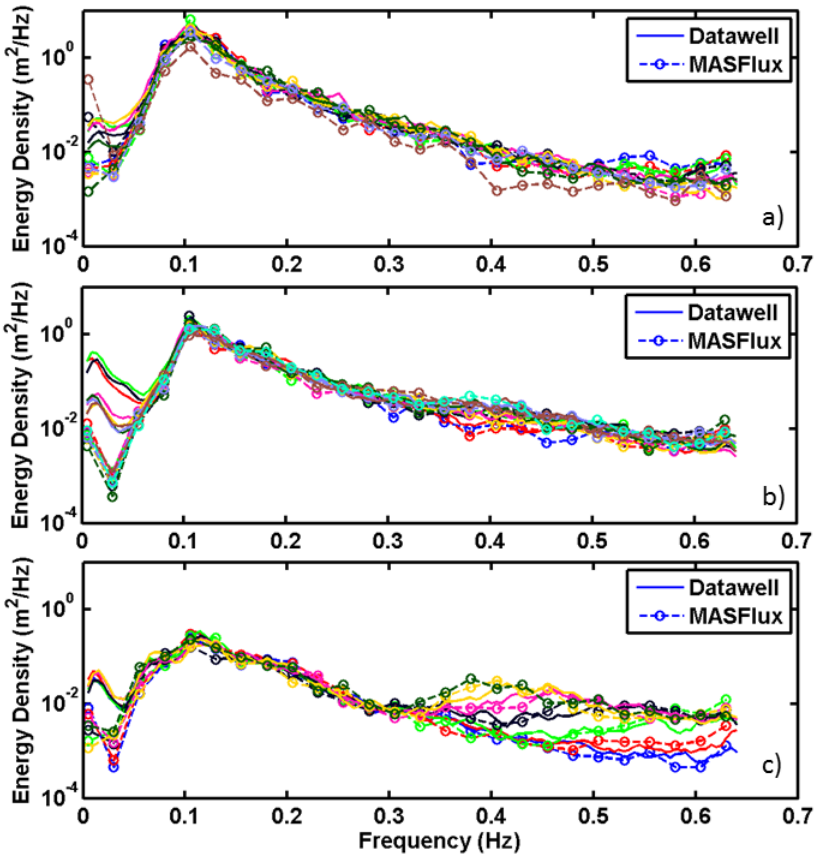

Figure 14. Wave energy spectra from measurements by DWR-G4 (solid line) and MASFlux (dash line and symbols) on (a) December 7, 2012, (b) April 19, 2013, and (c) May 3, 2013.

For directional spectra (Figure 15), data from both buoys agree well for most frequencies for December and April cruises (Figures 15a and 15b), but less agreement is seen for the May 3 case. This difference is attributed to the low wave energy observed on that day. However, in the frequency range with the most energetic waves, the wave direction spectra from both buoys are very

similar. Instrument noise would dominate the measurements where the wave energy is weak, as discussed in Alok et al. (1997) and Pearman et al. (2013).

During these three deployments only one change was made in the MASFlux configuration. The anti-rotational baffles shown in Figure 8 were moved some centimeters upward before the April cruise. This new set up was intended to minimize the rotational movement detected visually as well as in the VN-100 data.

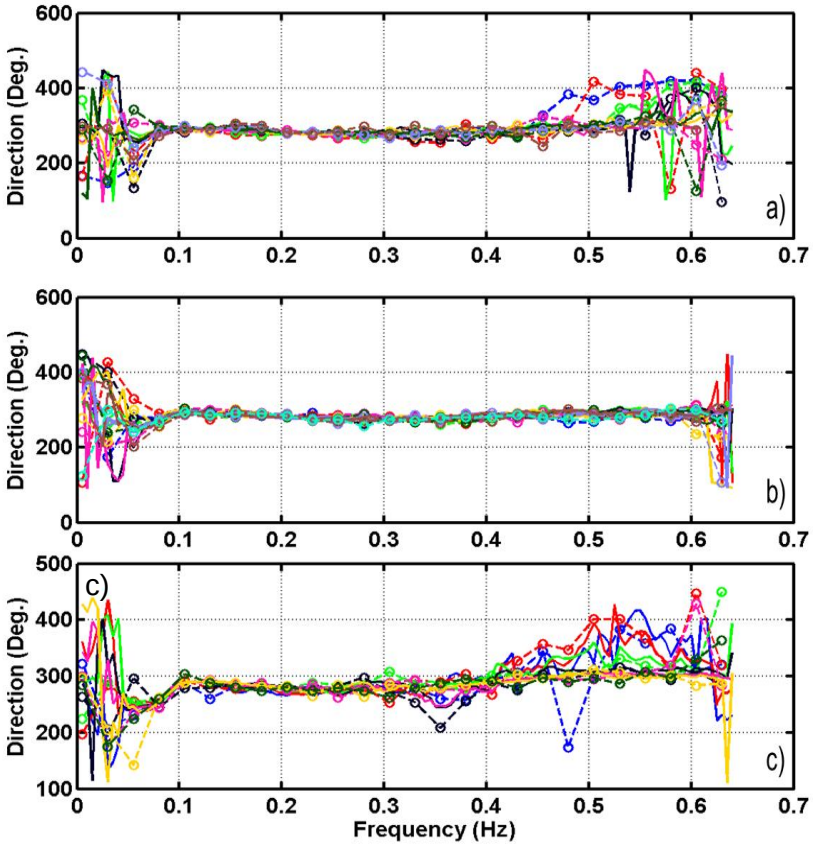

Figure 15. Spectra for wave direction measured by DWR-G4 (line only) and MASFlux (dash line and circle) during deployments on (a) December 7, 2012; (b) April 19, 2013, and (c) May 3, 2013. The legends are the same as in Figure 14.

The comparison of wave bulk parameters including significant wave height (SWH), dominant wave period (Tp), and direction of the spectral peak (DTp) are

shown in Figure 16. In Figure 16a the peak wave period is shown to be in the range of between 8 to 10 s. The spectral peak periods seem to compare well for most data segments except for three segments on December 7 when the discrepancies are relatively large, but the differences are still within 2 s.

The peak direction comparisons (DTp, Figure 16b) appear to be overestimated by the MASFlux in general. The difference is small where the maximum deviation is about 18 deg in only one case.

The SWH shows the best comparison (Figure 16 c) compared to other bulk parameters. On average, the discrepancies in SWH are less than 0.1 m. Also shown in Figure 16c, the difference in SWH from the two buoys decreases as the SWH becomes smaller. This trend needs to be validated with more at-sea measurements.

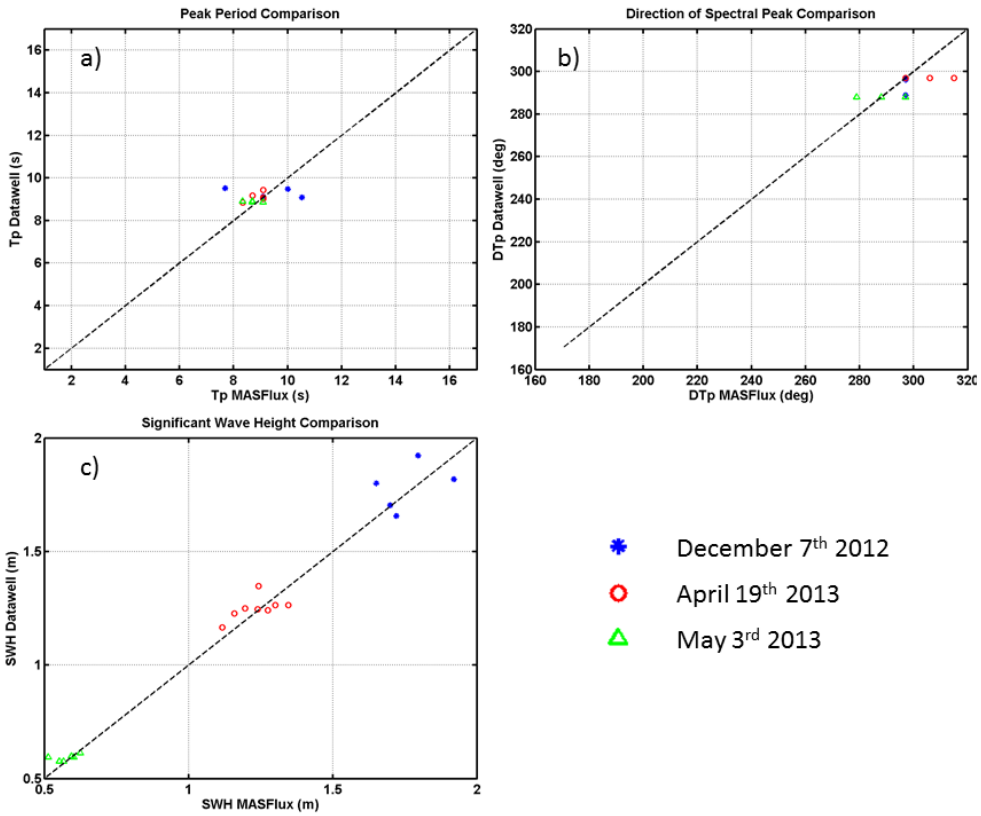

Figure 16. Comparison of wave bulk parameters between measurements from MASFlux and DWR-G4 buoys: a) Tp, b) DTp, and c) SWH.

B. ATMOSPHERIC TURBULENCE AND PROFILE MEASUREMENTS

1. Turbulent Power Spectra

Turbulent retrieval from a moving platform involves characterization of the platform motion and removes the effect of this motion on the flow measurements. This part of the work was done by NPS contractor, Dr. John Kalogiros. The results are examined in Figure 17, where the power spectra of the raw vertical wind component, from the 3-D sonic anemometer (green line), is compared with the retrieved vertical component of turbulence corrected for buoy motion (red line). The expected power spectra slope, the -5/3 slope, is shown on the figure for comparison purposes as well. If the turbulence field is adequately sampled, the turbulent inertial subrange should follow the -5/3 slope. This seems to be the case for the power spectra of the corrected vertical velocity. Figure 17a shows an evident peak near 0.1 Hz that is not present in the original sonic measurements. This peak frequency corresponds to the frequency of the dominant swell wave observed in the wave measurements (Figure 14). Since the MASFlux rides with the longer waves, the direct 3-D sonic measurements do not include perturbations at this frequency since the sonic measured the flow speed and direction relative to the sensor. The buoy motion, on the other hand, is recorded by the high sampling rate accelerometers and compass. The wave effect on the turbulence field thus shows up when the buoy motion is removed.

Comparisons of the power spectra for vertical velocity from different days appear to reaffirm the role of swell in generating the spectral peak at the frequency of the swell. The most prominent peak is found on December 7, 2012, when the swell SWH was the largest of the three days (Figure 17a). On the rest of the days (Figures 17b and 17c), when swell was not as strong as in the December case, the same peak is also observed corresponding to the swell frequencies with smaller magnitudes. The May 3, 2013, case has the weakest peak in the w power spectra. This case also has the smallest SWH (Figure 16).

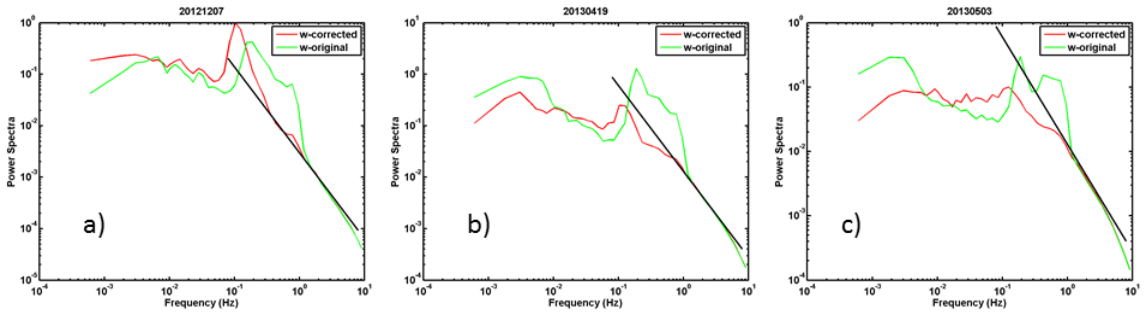

Figure 17. Power spectra of motion corrected (red) and original (green) vertical velocity (w) from the three test deployments. a) December 12, 2012; b) April 19, 2013; and c) May 03, 2013. The black line give a reference slope proportional to $f^{-5/3}$.

The power spectra of all motion corrected wind components are presented in Figure 18 with a reference line showing the slope of the $f^{-5/3}$ relationship of the power spectra in the inertial subrange. In all cases, as we can see, the effects of swell in the horizontal wind components are less in comparison to those in vertical velocity. This may have to do with the fact that horizontal wind components have rather significant energy in the longer wavelength as compared to vertical velocity. We also note the presence of less prominent peak in the spectra of the horizontal components at around 1.5 Hz, which is well into the inertial subrange as seen in the vertical velocity spectra. The presence of additional energy at this frequency is consistently seen on all three days. We suspect that this peak is related to the effect of the resonance of the buoy mast, which is caused by the flexibility of the mast. Future testing of the MASFlux will move the accelerometer up directly beneath the 3-D sonic anemometer to minimize its effects.

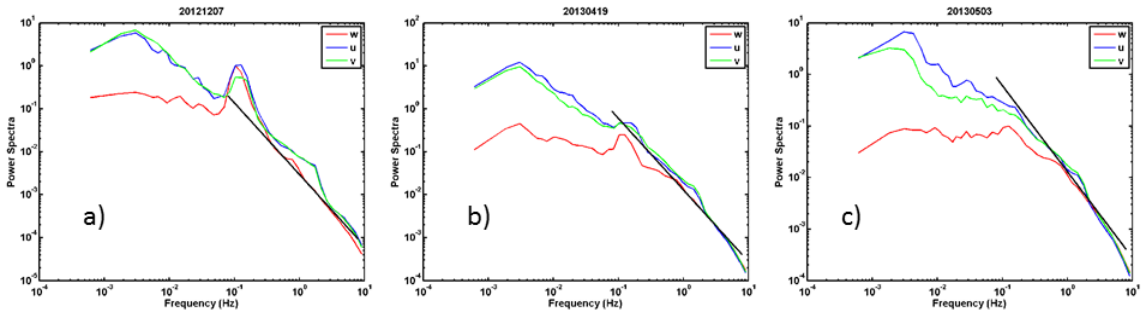

Figure 18. Horizontal (blue and green) and vertical (red) wind power spectra from a) December 12, 2012; b) April 19, 2013; and c) May 03, 2013.

2. Heat fluxes and Temperature Profiles

Different thermodynamic stratifications were encountered during the three test deployments analyzed in this study. The thermo stratification can be obtained from mean temperature and humidity measurements from four levels in the atmospheric surface layer, within less than 3.1 m height. The near surface water thermo stratification can be obtained from the three water temperature measurements within 0.5 m depth from the surface. As mentioned earlier in this chapter, temperature probes were calibrated before every deployment using the water bath method. It is important to note that calibration parameters did not vary from one deployment to the other.

The following discussion will demonstrate that the combined measurements from different components of the MASFlux can be used to reveal the characteristics of the near-surface processes. The measurements from the December deployment are shown in Figure 19. The evolution of the four levels of air temperature and three levels of water temperature are shown in Figure 19a. This case is characterized by cold air over warm water where the air-sea temperature difference is about 1.5 K. The vertical dash lines in Figure 19a denote the median of a 20-minute time period where the vertical profiles of temperatures were taken and shown in Figure 19b. The color of the profiles in Figure 19b corresponds to the median time denoted by the dashed line of the same color. The sensible heat flux is calculated from the motion corrected

vertical velocity and the virtual temperature from the 3-D ultrasonic anemometer at the top of MASFlux; its variation with time is shown in Figure 19c

The temporal variation of temperature at multiple levels (Figure 19a) seems to indicate a change of air mass at around 20:00 UTC, before which the thermo stratification in the lowest levels is much stronger than at the upper levels. This variation of the thermo stratification of the lowest levels is better seen in the temperature profiles averaged over a 20-minute period (Figure 19b). Figure 19b shows an extremely unstable near-surface layer from the first three 20-minute data segments. The lowest level temperature experienced significant cooling between 19:20 to 20:00 UTC over a nearly constant temperature upper ocean, which tends to enhance the instability of the lowest level. Thermo stratification between the two highest levels remains unstable in the earlier profiles, but showed signs of neutral to stable conditions towards the end of the deployment. The sensible heat flux, measured at the highest point of the MASFlux at 3.48 m height, remained positive throughout the measurement period, although the magnitude of the flux changed. This sign of the virtual heat flux is consistent with the air-sea surface temperature difference even though thermal stratification is different in the levels in between, and some of the local stratification is neutral or slightly stable in the overall unstable air-sea temperature setting.

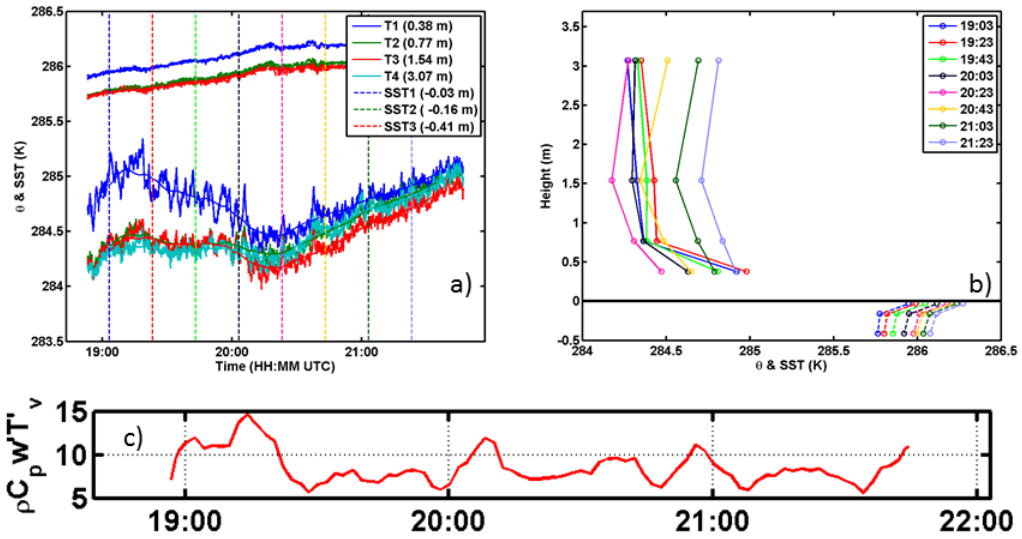

Figure 19. a) Potential and sea temperature time series, b) temperature profiles in the air and in the water, and c) sensible heat flux from December 7, 2012, dataset.

The case of April 19, 2013, is presented in Figure 20. This appears to be a simple case with well-defined and consistent unstable stratification at all levels (Figures 20a and 20b). The sign of observed surface virtual potential temperature flux is consistent with the bulk air-sea temperature difference as well as the stratification seen in the vertical profile of temperature. Also note that out of the three deployments, the magnitudes for heat fluxes are the highest in this case, which is consistent with the relatively large air-sea temperature difference.

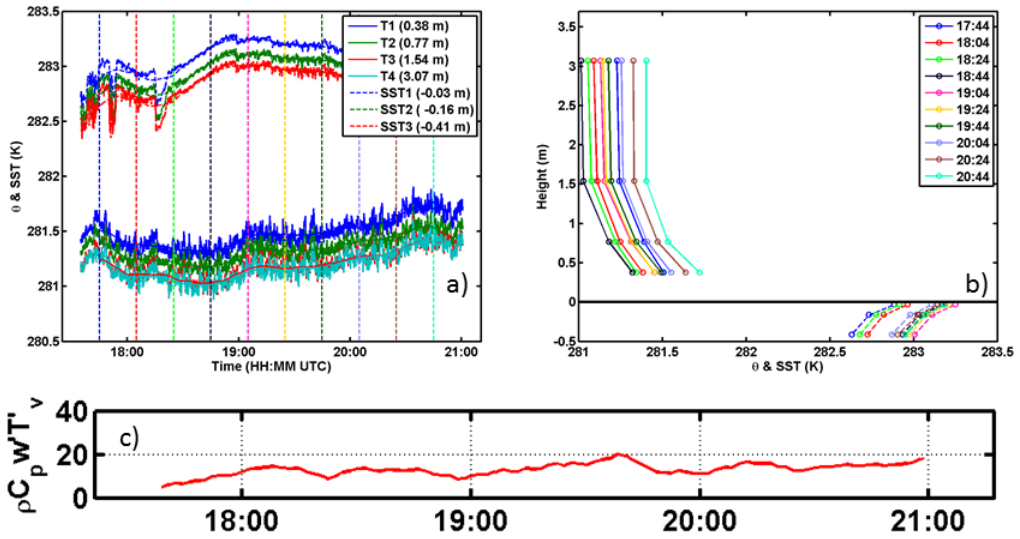

Figure 20. a) Time variation of potential and sea temperature time series; b) temperature profiles in the air and in the water; and c) sensible heat flux measured on April 19, 2013.

Similar presentation of data for May 03, 2013, measurements is shown in Figure 21. The gradual decrease of atmospheric potential temperature with time is shown in Figure 21a. Sea water temperature decreases during the first hour until around 19:00 UTC when the water temperature increases slowly. Towards the end of the measurements, the difference between the lowest atmospheric level and the top level sea water temperature is less than 0.3 K. Stable thermal stratification is evident in the vertical temperature profiles (Figure 21b) of all except for the last two. A change in the stability at the lowest levels is seen between 0.38 m to 0.77 m in the last two profiles. This reversal is coincident with the decrease in the air-sea temperature difference. The calculated heat flux ranges from -10 to -2 (Wm^{-2}). Although the lowest level has local unstable thermal stratification, the virtual heat flux, sampled at 3.5 m, remains negative, which is consistent with the stable thermal stratification at the height of the 3-D sonic anemometer.

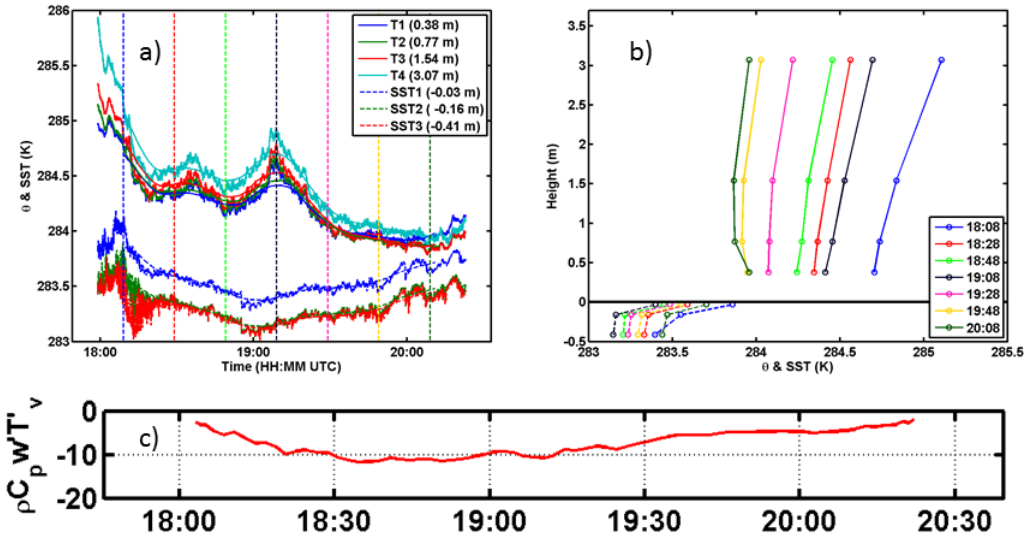

Figure 21. a) Temporal variation of potential temperature and sea water temperature; b) potential temperature profiles; and c) sensible heat flux from May 03, 2013, measurements.

3. Momentum Fluxes Representation

The data collected by the ultrasonic anemometer, located at 3.48 m above the sea level at the top of the MASFlux, resulted in measurements of the 3-D turbulence field and virtual temperature. These data can be used to obtain momentum flux (wind stress) using the direct eddy covariance method as well as the virtual heat flux as shown in the previous section. The mean wind speed and direction were collected by the two-dimensional sonic anemometers at 1.83 and 0.87 m above the sea level. Together with the 3-D sonic anemometer measurements at 3.48 m, we have the wind profiles at the lowest 3.5 m above the sea surface. Wind stress and the vertical mean wind profiles are the subject of discussion in this section. We will only discuss the measurements of December 7, 2012, and April 19, 2013, as examples.

Wind on the December test (Figure 22a) was the weakest of all three test days, where the strongest wind at the end of measurements was approximately 3 (ms^{-1}). Based on the wind profiles from MOST, we expected wind speed to increase with height from the surface. However, this is not the case observed on December 7, 2012. From the first three mean profiles (19:03, 19:23 and 19:43,

respectively), mean wind at the second level is in fact larger than the mean wind at the top 3-D sonic level. This observation can be attributed to the momentum transferred from the ocean to the atmosphere, which is the case of wave-driven wind. This observation is similar to early ones by Hanley et al. (2010). The temporal variation of the SWH on the same day is shown in Figure 23. It is clear that the profiles with wind reversal correspond to the time period with the strongest swell. Therefore, the connection between the wind reversal profiles and the wave field is clear.

Wind direction is found to change with time during the two-hour measurement period on December 7, 2012. Towards the end of the measurement period, the mean wind has a more westerly component.

The fairly small, but consistent, amount of wind stress from December 7, 2012, is shown in Figure 22c. These low stress values are consistent with the weak wind and stable stratification on this particular day. Surface stress ranges between 0.01 and 0.05 (Nm^{-2}).

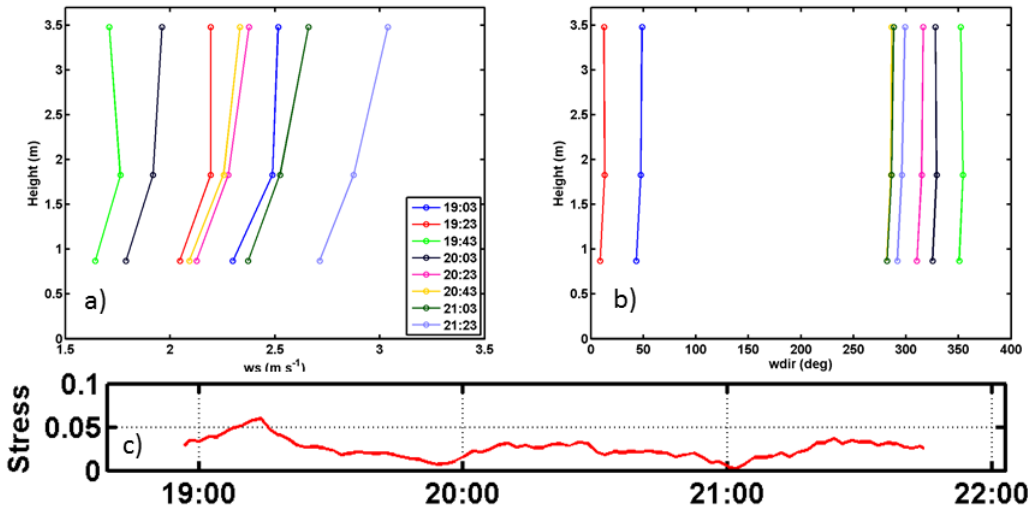

Figure 22. Measurements of a) mean wind speed; b) mean wind direction; and c) surface wind stress from December 7, 2012.

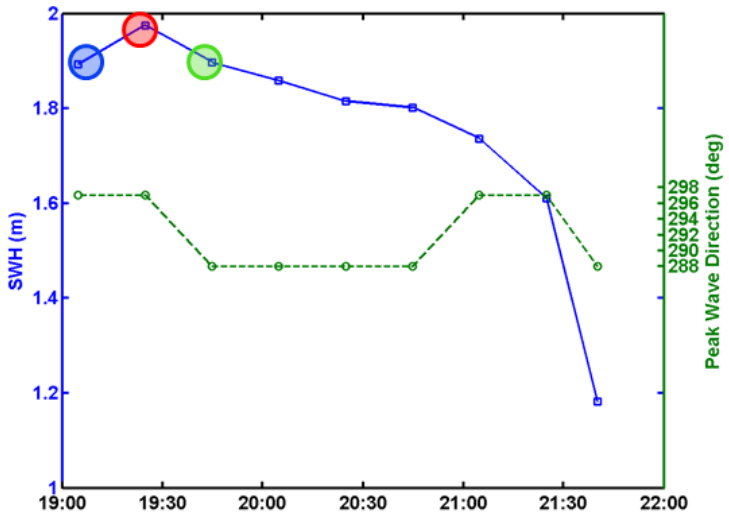

Figure 23. SWH (blue line) and DTp (green dashed line) plot from December 7, 2012, test. The blue, red and green circles denote concurrent SWH measurements when the same colored vertical profile was made at 19:03, 19:23 and 19:43, respectively.

The wind speed, direction, and wind stress on April 19, 2013, are shown in Figure 24. The low-level wind shear in magnitude and direction are apparent from these profiles. The mean wind on this day experienced some temporal variability where the lowest level wind varied between 3 and 5.5 ms^{-1}. It is also seen that the lowest 3 m or so of the atmosphere has some apparent wind shear (Figure 24b) where the wind direction changed from the lowest level to the top level (~2 m difference) by about 10 degrees. It is not clear whether this wind directional shear has to do with the forcing from the waves.

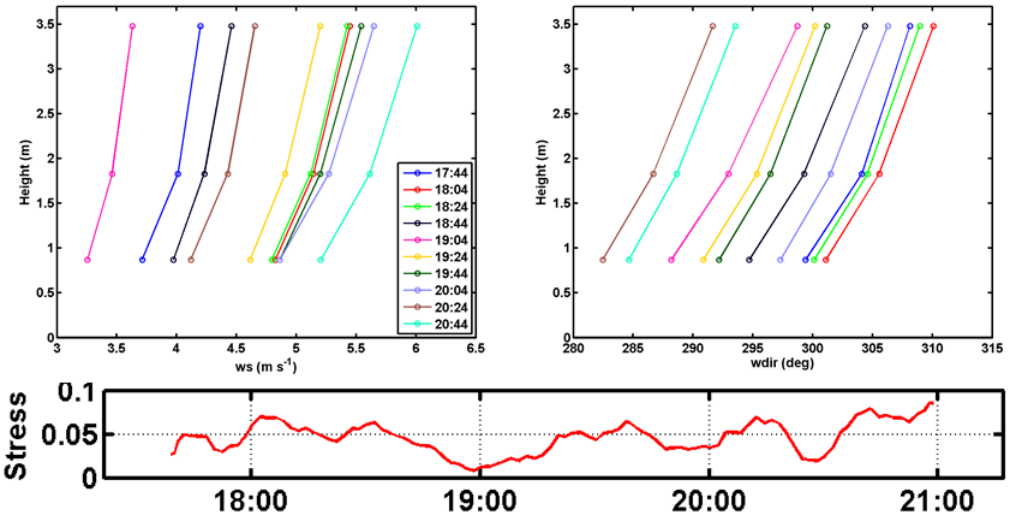

Figure 24. Same as in Figure 22, except for April 19, 2013.

V. CONCLUSIONS

The Meteorology Department of NPS has developed a small and easily deployable buoy system for concurrent measurements of the atmosphere and ocean near the air-sea interface. This system has evolved from the original buoy called Met-On-A-Stick (MOAS) presented by Cheney (2011). The most relevant upgrade is the sensors added, which provide concurrent wave and turbulent fluxes measurement capability. Such concurrent measurements are keys to further air-sea surface flux parameterization with explicit wave parameters.

The MASFlux system has a total length of 20 ft (~ 6 m) and weighs 40 kg. Sensors installed on the MASFlux are capable of measuring mean wind speed and direction at three levels, air temperature and relative humidity at four levels, sea water temperature at three water depth, atmospheric pressure at a single level, and three dimensional turbulence and virtual temperature at the top level. In addition, an accelerometer and an electronic compass deliver outputs needed for two-dimensional wave measurements.

Although there are other flux buoys that have similar or more measurement capability than the MASFlux, the small size and light weight of the MASFlux finds its niche in easy deployment and transport. During its test deployments, MASFlux deployment at sea was made onboard a 41-ft catamaran and needed only two-three people to set it off and recover it later. Its deployment does not require any special equipment which significantly increases the research opportunity using this buoy.

Measurements of the MASFlux from the initial at-sea deployment were analyzed in this thesis. For wave measurements evaluation, measurements from the DWR-G4 wave buoy were used as the ground truth. The DWR-G4 was deployed simultaneously with the MASFlux and the maximum distance between the two buoys was less than 100 m. Both directional and energy spectra from these buoys show very good agreement. The bulk parameters such as significant

wave height, peak period, and direction of the peak wave also show very good agreement with the DWR-G4 buoy. We thus conclude that the wave measurement from the MASFlux is as good as the DWR-G4 buoy.

Turbulence measurements from the ultrasonic anemometer were analyzed after the buoy motion was removed from the original measurements. The power spectra of vertical velocity shows clearly the -5/3 wavelength dependence in the turbulent inertial subrange. In all velocity spectra, a peak at the dominant swell frequency was identified on all test days and in all three wind components, denoting the effect of swell. A second peak was identified in the horizontal wind components at 1.5 Hz, which was thought to be related to the flexibility of the buoy mast. Future at-sea deployment will move the accelerometer closer to the 3-D sonic anemometer. These spectra analyses of the sonic anemometer measurements were helpful in identifying measurement issues related to platform motion.

The combined dataset from the MASFlux has proven to be effective in characterizing the atmospheric surface layer and the upper ocean. Comparison of the time evolution of the vertical profiles and the wave field reveals the role of the swell in providing momentum to the surface layer as evident from the wind profile with wind reversal in the lowest levels. We also saw that the sign of the surface heat flux is usually consistent with the overall air-sea temperature difference. However, the local gradient between the lowest two measurement levels is variable. This variability indicates the possible inadequacy of the MOST in applying it to the immediate air-sea interface.

LIST OF REFERENCES

Alok, K., P. R. de Jong, and S. R. Winterstein, 1997: Motions of a spar buoy in random seas: comparing predictions and model test results. *Delft Univ.*, 333–347.

Bao J.W., J. M. Wilczak, J.K. Choi, and L.H. Kantha, 2000: Numerical simulations of air-sea interaction under high wind conditions using a coupled model: a study of hurricane development. *Mon. Wea. Rev*., **128**, 2190–2210.

Bigorre S. P., R. E. Weller, J. B. Edson, and J. D. Ware, 2013: A surface mooring for air-sea interaction research in the Gulf Stream. Part II: Analysis of the observation and their accuracies. *J. Atmos. and Oceanic Technol.*, **30**, 450–469.

Burba, G. and D. Anderson, 2010: *A Brief Practical Guide to Eddy Covariance Flux Measurements*. Li-Cor Biosciences, 211 pp.

Businger, J. A., J. C., Wyngaard, Y. Izumi, and E. F. Bradley, 1971: Flux-profile relationships in the atmospheric surface layer. *J. Atmos. Sci.*, **28**, 181–189.

Breaker, L. C., and W. W. Broenkow, 1989: *The Circulation of Monterey Bay and Related Processes.* Moss Landing Marine Laboratories, 91 pp.

Charnock, H., 1955: Wind stress on a water surface. *Q. J. R. Meteorol. Soc.,* **81**, 639– 640.

Chen, S., T. J Campbell, H. Jin, S. Gabersek, R. Hodur, and P Martin, 2010*:* Effect of two-way air–sea coupling in high and low wind speed regimes. *Mon. Wea. Rev*., **138**, 3579–3602.

Chen, G., B. Chapron, R. Ezraty, and D. Vandemark, 2002: A global view of swell and wind sea climate in the ocean by satellite altimeter and scatterometer. *J. Atmos. and Oceanic Technol.,* **19**, 1849–1859.

Cheney, D. 2011: *Measurements of the Air-Sea Interface from an instrumented Small Buoy*, Naval Postgraduate School Thesis.

de las Heras, M.M. and P.A.E.M. Janssen, 1992: Data assimilation with a coupled wind-wave model. *J. Geophys. Res*., 97: 20,261—20,270.

de Vries, J. J., J. Waldron, and V. Cunningham, 2003: Field tests of the new Datawell DWR-G GPS wave buoy. *Sea Technol.*, **44**, 50–55.

Dobson, F. W., S. D. Smith, and R. J. Anderson, 1994: Measuring the relationship between wind stress and sea state in the open ocean in the presence of swell. *Atmosphere-Ocean*, **32**, 327–256.

Donelan, M. A., 1982: The dependence of the aerodynamic drag coefficient on wave parameters. *First Int. Conf. on Meteorology and Air–Sea Interaction of the Coastal Zone*, *The Hague*, Netherlands, Amer. Meteor. Soc., 381–387.

Donelan, M.A., 1990: Air–sea interaction. *The Sea*, *Vol. 9: Ocean Engineering Science*, B. Le Mehaute and D. M. Hanes, Eds., Wiley, 239–292.

Donelan, M.A.,E.W. Dobson, S.O. Smith and R.J. Anderson,1993: On the dependence of sea surface roughness on wave development. *J. Phys. Oceanogr*., **23**, 2143—2149.

Donelan, M. A., W. M. Drennan, and K. B. Katsaros, 1997: The air-sea momentum flux in conditions of wind sea and swell. *J. Phys. Oceanogr.,* **27**, 2087 - 2099.

Doyle, J.D. 1995*:* Coupled ocean wave/atmosphere mesoscale simulations of cyclogenesis. *Tellus,* 47A, 766–778.

Drennan, W. M., H. C. Graber, D. Hauser, and C. Quentin, 2003: On the wave age dependence of wind stress over pure wind seas. *J. Geophys. Res.*, **108(C3)**, 8062, doi:10.1029/2000JC000715.

Drennan, W. M., K. K. Kahma, and M. A. Donelan, 1999: On momentum flux and velocity spectra over waves. *Bound.-Layer Meteor.,* **92**, 489–515.

Edson, J. B., A. A. Hinton, K. E. Prada, J. E. Hare, and C. W. Fairall, 1998: Direct Covariance Flux Estimates From Mobile Platforms at Sea. *J. Atmos. and Oceanic Technol.*, **15**, 547– 562.

Eymard, L., G. Caniaux, H. Dupuis, L. Prieur, H. Giordani, R. Troadec, P. Bessemoulin, G. Lachaud, G. Bouhours, D. Bourras, C. Guerin, P. Le Borgne, A. Brisson, and A. Marsouin, 1999: Surface fluxes in the North Atlantic current during CATCH/FASTEX. *Q. J. R. Meteor. Soc*., **125**, 3562–3599.

Fairall C. W., J. B. Edson, S. E. Larsen, and P. G. Mesteyer, 1990: Inertial-dissipation air-sea flux measurements: A prototype system using real-time spectral computations. *J. Atmos. and Oceanic Technol.*, **7**, 425– 453.

Fairall C. W., E. F. Bradley, D. P Rogers, J. B. Edson, and G. S. Young, 1996: Bulk parameterization of air-sea fluxes in TOGA COARE. *J. Geophys. Res.*, **101**, 3747–3767.

Fairall C. W., E. F. Bradley, J. E. Hare, A. A. Grachev, and J. B. Edson, 2003: Bulk parameterization of air-sea fluxes: Updates and verification for COARE algorithm. *J. of Climate*, 16, 571–591.

Fisher F. H., and F. N. Spiess, 1963: FLIP-floating instrument platform. *J. Acoust. Soc. Am.*, **35**, 1633–1644.

Frederickson, P. A. and K. L. Davidson, 2003: Observational buoy studies of coastal air-sea fluxes. *J. of Climate*, 16, 593 – 599.

Geernaert, G. L., K. B. Katsaros, and K. Ritcher, 1986: Variation of the drag coefficients and its dependence on sea state. *J. Geophys. Res*., **91**, 7667–7679.

Geernaert, G.L., S.E. Larsen, and F. Hansen, 1987: Measurements of the wind stress, heat flux, and turbulence intensity during storm conditions over the North Sea. *J. Phys. Oceanogr*., **92**, 13,127–13,139.

Grachev, A. A., and C. W. Fairall, 2001: Upward momentum transfer in the marine boundary layer*. J. Phys. Oceanogr.,* **31**, 1698–1711.

Graber, H.C., M. A. Donelan, W. M. Drennan, and J. C. Van Leer, 2000: ASIS – A new air-sea interaction spar buoy: design and performance at sea*. J. Atmos. and Oceanic Technol.,* 17, 708 – 720.

Hanley, K. E., S. E. Belcher, and P. P. Sullivan, 2010: A global climatology of wind–wave interaction*. J. Phys. Oceanogr.,* 40, 1263–1282.

Herbers, T. H. C., P. F. Jessen, T. T. Janssen, D. B. Colbert, and J. H. MacMahan, 2011: Observing Ocean Surface Waves with GPS-Tracked Buoys. *J. of Atmos. and Oceanic Technol.,* **29**, 944–959.

Holland, J. Z., W. Chen, J. A. Almazon, and F. C. Elder, 1981: Atmospheric boundary layer. *In IFYGL* (E. J. Aubert, and T. L. Richards eds.), 147 pp.

Hornick, H. R., 2012: *Evolution of atmosphere and ocean boundary layers from aircraft observations and coupled COAMPS/NCOM*, Naval Postgraduate School PhD Thesis.

Janssen, P.A.E.M., 1999: On the effect of ocean waves on the kinetic energy balance and consequences for the inertial dissipation technique. *J. Phys. Oceanogr.,* **29**, 530–534.

Jones, I. S. F., and Y. Toba, 2001: *Wind Stress Over the Ocean.* Cambridge University Press, 307 pp.

Kawai, Y., and A. Wada, 2007: Diurnal sea surface temperature variation and its impact on the atmosphere and ocean: a review. *J. Oceanogr.,* **58**, 805–814.

Kraus E. B., and J. A. Businger, 1994: *Atmosphere-Ocean Interaction*. Oxford University Press, 384 pp.

Lykossov, V. V., 2001*: Atmospheric and Oceanic Boundary Layer Physics, in Wind Stress over the Ocean*, Ian S.F. Jones and Y. Toba, eds., Cambridge University Press, 54–81.

Massel, S. R., 1996: *Ocean Surface Waves: Their Physics and Prediction*. World Scientific, 491 pp.

Monin, A. S., and A. M. Obukhov, 1954: Basic laws of turbulent mixing in the surface layer of the atmosphere. *Tr. Akad. Nauk SSSR Geofiz. Inst*., **24**, 163–187.

National Data Buoy Center (1996): Nondirectional and directional wave data analysis procedures. *Technical Report 96–01*, 43.

Pearman, D. W., T. H. C. Herbers, T. T. Janssen, S. F. McIntyre, and P. F. Jessen, 2013: GPS and accelerometer equipped drifters for observing ocean surface waves and currents. Continental Shelf Res., in review.

Perrie, W., and B. Toulany, 1990: Fetch relations for wind-generated waves as a function of wind stress scaling. *J. Phys. Oceanogr.*, **20**, 1666–1681.

Pierson, W. J., Jr., and L. Moskowitz, 1964: A proposed spectral form for fully developed wind seas based on the similarity theory of S. A. Kitaigorodskii. *J. Geophys. Res.,* **69**, 5181–5190.

Smith, S. D., R. J. Anderson, W. A. Oost, C. Kraan, N. Maat, J. de Cosmo, K. B. Katsaros, K. L. Davidson, K. Bumke, L. Hasse, and H. M. Chadwick, 1992: Sea surface wind stress and drag coefficients: the HEXOS results. *Boundary Layer Meteor*., **60**, 109– 142.

Stewart, R. W., 1974: The air-sea momentum exchange. *Bound.-Layer Meteor.,* **6**, 151–167.

Volkov, Yu. A., 1968: *An experimental study of the characteristics of turbulence in the marine surface layer and wind-driven waves*. Ph.D. thesis, Institute of Oceanology, Russian Academy of Science, Moscow, Russia, 132 pp.

Webster, P. J., and R. Lukas, 1992: TOGA COARE: The coupled ocean atmosphere response experiment*. Bull. Amer. Meteor. Soc.,* **73,** 1377 – 1416.

Weller, R. A., S. P. Bigorre, J. Lord, and J. D. Ware, 2012: A surface mooring for air-sea interaction research in the Gulf Stream. Part I: Mooring design and instrumentation. *J. Atmos. and Oceanic Technol.*, **29**, 1363–1376.

Yelland, M., and P. K. Taylor, 1996: Wind stress measurements from the open ocean*. J. Phys. Oceanogr*., **26**, 541–558.

THIS PAGE INTENTIONALLY LEFT BLANK

INITIAL DISTRIBUTION LIST

1. Defense Technical Information Center
   Ft. Belvoir, Virginia

2. Dudley Knox Library
   Naval Postgraduate School
   Monterey, California